

UNIVERSITÉ DU QUÉBEC À RIMOUSKI

**L'IMPACT DU COUVERT DE GLACE SUR LA STRUCTURE  
TURBULENTE DES ÉCOULEMENTS DANS UN MÉANDRE DE  
LA RIVIÈRE NEIGETTE**

MÉMOIRE  
PRÉSENTÉ COMME EXIGENCE PARTIELLE  
DE LA MAÎTRISE EN GÉOGRAPHIE  
EXTENSIONNÉE DE  
L'UNIVERSITÉ DU QUÉBEC À MONTRÉAL

PAR  
SYLVIO DEMERS

JANVIER 2011

UNIVERSITÉ DU QUÉBEC À RIMOUSKI  
Service de la bibliothèque

Avertissement

La diffusion de ce mémoire ou de cette thèse se fait dans le respect des droits de son auteur, qui a signé le formulaire « *Autorisation de reproduire et de diffuser un rapport, un mémoire ou une thèse* ». En signant ce formulaire, l'auteur concède à l'Université du Québec à Rimouski une licence non exclusive d'utilisation et de publication de la totalité ou d'une partie importante de son travail de recherche pour des fins pédagogiques et non commerciales. Plus précisément, l'auteur autorise l'Université du Québec à Rimouski à reproduire, diffuser, prêter, distribuer ou vendre des copies de son travail de recherche à des fins non commerciales sur quelque support que ce soit, y compris l'Internet. Cette licence et cette autorisation n'entraînent pas une renonciation de la part de l'auteur à ses droits moraux ni à ses droits de propriété intellectuelle. Sauf entente contraire, l'auteur conserve la liberté de diffuser et de commercialiser ou non ce travail dont il possède un exemplaire.

## *REMERCIEMENTS*

D'abord, merci au chef d'orchestre, Thomas Buffin-Bélanger. Il est celui qui, par son imagination et son enthousiasme contagieux, a initié et canalisé mon intérêt académique. Merci aussi à André Roy, co-directeur du projet, pour sa patience, mais surtout sa capacité à apporter un solide soutien en toute circonstance malgré les silences radios prolongés dans l'avancement du projet.

Mille mercis à tous ceux qui ont transformé le défi terrain en réalité malgré des conditions de travail souvent indécentes. J'ai nommé : Geneviève Allard, Étienne Bachand, Frédéric Banville, Jérôme Bossé, Vincent Bélanger, Louise-Anne Belzile, Marc Desrosiers, Jérôme Dubé (et son gin chaud), Michel Grégoire, Roch Guèvremont, Yanick Larue, Dany Lechasseur, Marie-André Lelièvre, Taylor Olsen, Dany Picard, François Saint-Pierre, Pierre Simard, Benoit Talbot, Suzan Taylor, Simon Tolszczuk et Benoît Vigneault. Je prends comme un honneur personnel le soutien qui m'a été accordé pendant cette période. Un merci spécial à tous ceux qui ont poussé la bête sur les berges de la Neigette et à ceux qui ont réussi à repêcher la perceuse à glace alors que j'étais prêt à l'abandonner sur place. Exploit mémorable. Merci à Normand Bergeron pour le prêt de ladite perceuse et à Innovations Maritime pour le prêt gratuit et en toute confiance de matériel onéreux. Merci aux ingénieurs Taylor Olsen, François Truchon et Karl Turcotte qui ont travaillé en vrais professionnels pour développer les instruments de travail. Vos réalisations parlent d'elles-mêmes.

Un large merci aux membres du Laboratoire de dynamique fluviale de Rimouski et de la Chaire de recherche du Canada en dynamique fluviale de l'Université de Montréal qui m'ont accueilli. Merci à Geneviève Marquis qui m'a fait progresser de manière exponentielle dans mon apprentissage de Matlab ainsi qu'à Annie Cassista qui a partagé sa connaissance d'un instrument pour le moins mystique et ses programmes de traitement de données pour le gérer.

Sans vous deux, j'en serais encore à l'étape de filtrer des séries de vitesses avec Excel. Évidemment, merci à ma blonde Susan Drejza, qui m'a secondé dans toutes les étapes de réalisation du mémoire : réflexion, terrain, traitement, mise en page, révision. Merci aussi à la famille qui a fourni un support moral et financier qui remonte aux ères géologiques de mon existence, sans quoi je serais aujourd'hui quelque chose comme un mécanicien aux tendances turbulentes. Enfin, merci aux bailleurs de fonds du projet, principalement le Conseil de recherche en sciences naturelles et en génie (CRSNG) et les Fonds institutionnel de recherche (FIR).

## *TABLE DES MATIÈRES*

<i>LISTE DES FIGURES</i> .....	<i>vi</i>
<i>LISTE DES TABLEAUX</i> .....	<i>viii</i>
<i>LISTE DES ABRÉVIATIONS, SIGLES ET ACRONYMES</i> .....	<i>ix</i>
<i>LISTE DES SYMBOLES</i> .....	<i>x</i>
<i>RÉSUMÉ</i> .....	<i>xii</i>
<i>INTRODUCTION</i> .....	<i>1</i>
<i>CHAPITRE I</i>	
<i>MACROTURBULENT COHERENT STRUCTURES IN ICE-COVERED RIVER FLOW USING A PULSE-COHERENT ACOUSTIC DOPPLER PROFILER</i> .....	<i>5</i>
<i>1.1 Introduction</i> .....	<i>8</i>
<i>1.2 Methodology</i> .....	<i>11</i>
<i>1.2.1 Experimental design</i> .....	<i>11</i>
<i>1.2.2. Data validation</i> .....	<i>13</i>
<i>1.2.3. Data analyses</i> .....	<i>16</i>
<i>1.3. Results</i> .....	<i>21</i>
<i>1.3.1. Mean and turbulent parameters</i> .....	<i>21</i>
<i>1.3.2. Visualization of macroturbulent coherent flow structures</i> .....	<i>23</i>
<i>1.3.3. Integral time and length scales of macroturbulence</i> .....	<i>27</i>
<i>1.3.4. Inclination of macroturbulent structures</i> .....	<i>29</i>
<i>1.3.5. Correlation matrices</i> .....	<i>31</i>
<i>1.4. Discussion</i> .....	<i>35</i>

<b>CHAPITRE II</b>	
<b>HELICAL CELL MOTIONS IN A SMALL ICE-COVERED MEANDER RIVER REACH</b>	<b>41</b>
.....	.....
<b>2.1. Introduction</b> .....	43
<b>2.2. Methodology</b> .....	44
<b>2.3. Results</b> .....	47
2.3.1. Ice cover and velocity profiles .....	47
2.3.2. Three dimensional flow pattern .....	49
<b>2.4. Discussion</b> .....	55
<b>CONCLUSION</b> .....	58
<b>RÉFÉRENCES</b> .....	60

## *LISTE DES FIGURES*

Figure 1 : a) Microformes sous un bloc de glace découpé en rivière; b) schéma théorique de l'effet de la présence d'un couvert de glace sur la structure de la CLT et c) schéma théorique des écoulements secondaires sous glace dans un méandre de rivière selon les études en laboratoire. ....	2
Figure 1.1: a) Sampling scheme in the Neigette River and b) setup parameters of the PC-ADP. ....	11
Figure 1.2 : Percentage of data corrected per time series using (1) the algorithm of ambiguity correction (light gray) and (2) the de-spiking algorithm (dark gray). Black stripes (3) identify time series entirely removed.....	14
Figure 1.3: a) Velocity time series as collected by the PC-ADP after data validation, b) binary representation of the velocities from their deviance from the mean and c) identification of clusters of coherent motions in the flow from the LISA algorithm .	20
Figure 1.4: a) Velocity profiles and b) Reynolds shear stress for profiles measured during open (p0) and ice-covered flow conditions (p1; p2; p3; p4). ....	22
Figure 1.5: Clusters of coherent motions as revealed by the LISA algorithm when applied to the $u$ component of the flow.....	25
Figure 1.6: Clusters of coherent motions as revealed by the LISA algorithm when applied to the $v$ component of the flow.....	26
Figure 1.7: Integral time scales and integral length scale of open channel and ice covered flow conditions for the $u$ and $v$ components of the flow .....	28
Figure 1.8: Isolines of cross-correlation values between the top third cell from the water surface (or ice cover) and every other downward cells of the profiles. ....	31
Figure 1.9: Correlation values between the time series of the profile for the a) $u$ and b) $v$ component of the flow.. .....	33

Figure 1.10: Conceptual model of macroturbulent coherent structures under an ice cover.....	39
Figure 2.1 : a) Meander reach sampling scheme; b) PC-ADP sampling scheme. ....	45
Figure 2.2 : Ice cover thickness and undercover roughness for the 2007 and 2008 surveys. ....	48
Figure 2.3 : Velocity profiles at the entrance of pool for the 2007 and 2008 surveys. ....	49
Figure 2.4 : Planform view of depth-averaged flow velocities of the 2008 survey....	50
Figure 2.5 : Longitudinal and secondary flow patterns viewed downstream from bottom to top (2008 survey).....	53
Figure 2.6 : Frazil ice obstruction and flow velocities in the pool area of the 2007 survey .....	54

*LISTE DES TABLEAUX*

Table 1.1 : Physical characteristics at velocity profiles sampling location.....	12
Table 1.2: Correspondences of mean and turbulent parameters as measured by the PC-ADP when compared to the ADV .....	17
Table 1.3: Dimensionless depths of the plane of maximal velocities and zero Reynolds shear stress .....	22
Table 1.4: Mean correlation coefficients and vertical extension of correlated cells in the flow.....	34

*LISTE DES ABRÉVIATIONS, SIGLES ET ACRONYMES*

ACF	Autocorrelation function
ADV	Acoustic Doppler Velocimeter
CLT	Couche-Limite Turbulente
CS	Cross-Section
ILS	Integral Length Scale
ITS	Integral Time Scale
LISA	Local Indicator of Spatial Association
LSR	Least Square Regression
PC-ADP	Pulse Coherent Acoustic Doppler Profiler
SNR	Signal to Noise Ratio
TBL	Turbulent Boundary Layer

## *LISTE DES SYMBOLES*

$c$	Vitesse du son dans l'eau (m/s)
$c_{u_1-u_2}$	Covariance entre deux séries temporelles
$d$	Distance entre deux cellules du profil (m)
$d_{\text{corr}}$	Distance à l'intérieur de laquelle deux séries temporelles possèdent une corrélation significative (m)
$F$	Fréquence
$N$	Nombre d'objets dans une série temporelle
$p_{\text{max}}$	Longueur du profil du PC-ADP (m)
$p_{\text{res}}$	Longueur du profil jusqu'à la cellule de résolution (m)
$r$	Coefficient de corrélation de Pearson
$s_u$	Écart-type des fluctuations de vitesses dans la composante longitudinale
$s_v$	Écart-type des fluctuations de vitesses dans la composante verticale
$s_w$	Écart-type des fluctuations de vitesses dans la composante latérale
$u'$	Fluctuations de vitesse dans la composante longitudinale (m/s)
$u_i$	Vitesses instantanées dans la composante longitudinale (m/s)
$\bar{u}$	Vitesse moyenne dans la composante longitudinale (m/s)
$V_A$	Vitesse d'ambiguïté (m/s)
$V_p$	Vitesse des particules (m/s)
$v'$	Fluctuations de vitesse dans la composante verticale (m/s)
$v_i$	Vitesses instantanées dans la composante verticale (m/s)
$\bar{v}$	Vitesse moyenne dans la composante verticale (m/s)
$w'$	Fluctuations de vitesse dans la composante latérale (m/s)
$w_i$	Vitesses instantanées dans la composante latérale (m/s)
$\bar{w}$	Vitesse moyenne dans la composante latérale (m/s)

x	Coordonnées cartésiennes (longitudinal)
Y	Profondeur de l'eau (m)
y	Coordonnées cartésiennes (vertical)
$y_{u_{\max}}$	Profondeur d'eau des vitesses maximales dans la composante longitudinale
$y_{uv=0}$	Profondeur d'eau où $-\rho \overline{u'v'} = 0$
z	Coordonnées cartésiennes (latéral)
$\rho$	Densité de l'eau
$\varphi$	Angle d'inclinaison des structures à grande échelle
$\Delta L_{\max}$	Décalage temporel du maximum de corrélation entre deux séries temporelles (s)
$\Delta t$	Différence de temps (s)
$\Delta \Phi$	Différence de phase

## *RÉSUMÉ*

Le couvert de glace impose une rugosité de surface qui modifie la structure des écoulements turbulents en rivière. Deux gradients de vitesses apparaissent, l'un associé à la rugosité du lit et l'autre à celle de la glace. L'impact d'un écoulement composé de deux couches-limites sur les échanges turbulents en rivière est appréhendé à deux échelles : 1) celle du développement des structures macroturbulentes et 2) celle du patron des écoulements secondaires dans une section de rivière à méandres. Ces deux échelles sont en apparence distinctes par le large écart des dimensions de temps et d'espace qui sont impliquées, mais toutes deux sont directement affectées par une structure de l'écoulement composée de deux couches-limites. Des données de vitesses d'écoulement ont été mesurées avec un profileur acoustique à effet Doppler pendant deux hivers successifs dans un méandre de la rivière Neigette (Rimouski, Québec). À l'échelle des profils de vitesses, des structures macroturbulentes sous la forme de bandes verticales de basses et de hautes vitesses sont observées. En l'absence de glaces, elles peuvent occuper toute la profondeur de l'écoulement alors qu'en présence d'un couvert de glace elles sont préférentiellement situées à proximité des plans de rugosité et se raréfient dans la région centrale de l'écoulement. En conséquence, la taille des structures est considérablement réduite dans leur extension longitudinale et verticale. Il est suggéré que chaque plan de rugosité initie des structures macroturbulentes et que celles-ci se rencontrent au centre de l'écoulement où elles se confrontent et se dissipent. Elles peuvent occuper simultanément les deux-couches limites, mais sont moins fréquentes et plus éphémères que celles qui sont observées en l'absence de couvert de glace. À l'échelle du méandre, l'analyse du patron spatial des écoulements secondaires révèle la présence de deux cellules hélicoïdales à l'entrée de la courbure. À l'apex, une seule cellule avec un sens de rotation inverse à celui attendu dans des conditions libres de glace est observée. Le patron des écoulements secondaires de la rivière Neigette est plus complexe que la référence conceptuelle basée sur des résultats de laboratoire où figurent deux cellules hélicoïdales stables à travers l'ensemble du méandre. Cette différence est expliquée par une morphologie naturelle plus complexe ainsi que par le jeu des interactions entre les deux cellules hélicoïdales. La présence d'accumulation de frasil dans le méandre lors du premier hiver révèle que les écoulements secondaires se développent quasi-instantanément à la sortie de la zone obstruée. Ces résultats mettent en évidence l'étendue des impacts associés à la présence d'un couvert de glace et insiste sur le large éventail des échelles qui sont impliquées. Cette étude fournit des observations originales qui permettent d'initier un questionnement mieux dirigé à propos des impacts du couvert de glace sur la structure turbulente des écoulements en rivière.

**Mots clés** : couvert de glace, couche-limite turbulente, structures macroturbulentes, écoulements secondaires, cellules hélicoïdales, profileur acoustique à effet Doppler

## ***INTRODUCTION***

Dans les climats tempérés froids, l'hiver est souvent perçu comme une période d'accalmie pour les systèmes fluviaux. Les chenaux sont couverts d'une couche de glace qui paralyse en apparence l'activité fluviale. Or, la période hivernale engage un enchaînement de nouveaux processus et de formes qui modifient en profondeur les interactions dans le système fluvial (Allard *et al.*, 2009). Le couvert de glace est un volume solide qui confine l'écoulement dans un conduit fermé. L'envers du couvert de glace est souvent moins lisse qu'il n'y paraît sur la surface et peut présenter des microformes profilées à l'image des rides sableuses ou des aspérités liées à la fusion de la glace (figure 1a). La présence d'un couvert de glace plus ou moins rugueux ralentit l'écoulement en surface et forme un second gradient de vitesse. En conséquence, l'écoulement sous glace est caractérisé par deux couches-limites turbulentes (figure 1b), l'une propre au lit (CLT<sub>l</sub>) et une seconde liée à la glace (CLT<sub>g</sub>). L'impact de cette structure de l'écoulement dans la nature des échanges turbulents en milieu fluvial reste toutefois largement inexploré.

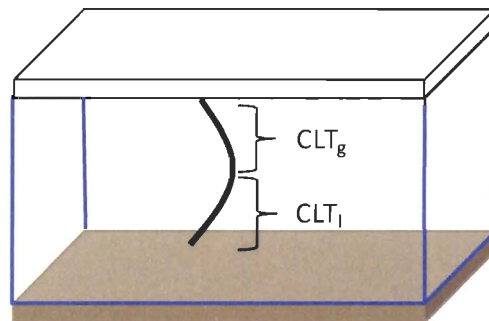
Depuis la deuxième moitié du XX<sup>ème</sup> siècle, des structures cohérentes de fluide avec des cycles de vie quasi-périodiques ont été observées dans des écoulements en laboratoire et en rivière. Parmi elles, on distingue celles dites macroturbulentes dont la taille est proportionnelle à la profondeur de l'écoulement. Ce sont des échanges cohérents de fluide qui, en rivière de petite et moyenne tailles, dominent la totalité de la tranche de l'écoulement. Pendant la période hivernale, l'interaction de l'écoulement avec la rugosité glacielle produit une nouvelle source de turbulence. Cette turbulence est associée à des échanges cohérents émanant du couvert de glace qui se propagent dans l'écoulement et se mélangent aux structures en provenance du lit. L'effet de cette double CLT sur l'occurrence des échanges macroturbulents est inconnu. Cette méconnaissance provient autant d'un manque d'acquis sur

les mécanismes spécifiques à la formation des structures macroturbulentes qu'à une absence d'étude portant spécifiquement sur cette échelle.

a)



b)



c)

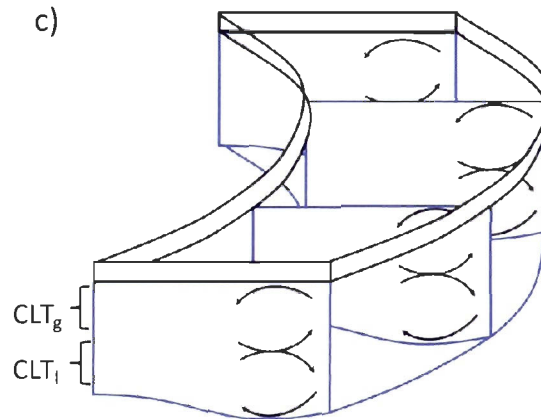


Figure 1 : a) Microformes sous un bloc de glace découpé en rivière; b) schéma théorique de l'effet de la présence d'un couvert de glace sur la structure de la CLT et c) schéma théorique des écoulements secondaires sous glace dans un méandre de rivière selon les études en laboratoire.

À l'échelle des tronçons fluviaux, les échanges turbulents se traduisent par des patrons tridimensionnels complexes. Le patron spatial des écoulements secondaires dans les méandres à surface libre est bien connu et se résume grossièrement à la présence d'une cellule de rotation hélicoïdale (Blanckaert et Graf, 2001; Frothingham et Rhoads, 2003). Ce schéma conceptuel est toutefois inapplicable aux conditions englacées en raison de la nouvelle structure de la CLT. Des études en laboratoire ont montré que le patron spatial des écoulements dans les chenaux curvilinéaires avec couvert de glace présentent deux cellules hélicoïdales superposées et de sens de rotation inverse (figure 1c) (Zufelt, 1988; Urroz et Ettema, 1994). Toutefois, les simulations en laboratoire simplifient les conditions naturelles caractérisées par une morphologie complexe et l'effet potentiel des accumulations de frasil sous le couvert. Les accumulations de frasil sont courantes pendant la période hivernale et peuvent générer des obstructions majeures à l'écoulement. La constriction des écoulements peut même être suffisante pour générer la mobilisation des sédiments et modifier les formes du lit (Sui *et al.*, 2008).

Cette étude se base sur un échantillonnage du champ de vitesses dans un méandre de la rivière Neigette, située en périphérie de la ville de Rimouski (Québec, Canada). Les mesures de vitesses ont été obtenues à l'aide d'un profileur acoustique à effet Doppler (PC-ADP). Celui-ci mesure des séries temporelles de vitesses simultanément sur l'ensemble de la profondeur et dans les trois dimensions de l'espace. C'est un instrument non-intrusif adapté aux rivières peu profondes et suffisamment robuste pour résister aux températures hivernales. Les capacités du PC-ADP offrent une opportunité unique pour l'étude des structures macroturbulentes dans l'écoulement sans avoir recours à une série de sondes ponctuelles intrusives, donc plus délicates à déployer sous un couvert de glace en rivière. Aussi, cette simultanéité dans l'acquisition des séries temporelles accélère la collecte de données et permet de reconstituer le champ tridimensionnel des vitesses d'écoulement à l'échelle d'un tronçon fluvial en relativement peu de temps. Trois campagnes de terrain ont eu lieu, deux pendant les hivers 2007 et 2008 et une pendant l'été 2007, ce qui a permis l'acquisition de plus d'une centaine de profils de vitesses. Pendant l'hiver 2007, le méandre était occupé par une quantité importante de frasil qui modifiait le patron des écoulements dans le méandre et

empêchait localement l'acquisition des données par le PC-ADP. En 2008, le frazil était absent. Ce qui est apparu en premier lieu comme un obstacle majeur au projet a été en définitive exploité pour étudier l'effet des engorgements de frazil sur le patron de vitesses par une analyse comparative entre les données de l'hiver 2007 et 2008.

Le mémoire comprend deux chapitres, chacun sous forme d'article visant à être soumis à un périodique scientifique :

- 1) Le premier article est intitulé *Structures macroturbulentes mesurées à l'aide d'un profileur acoustique à effet Doppler dans une rivière avec couvert de glace* (traduction de l'auteur). L'article porte sur une analyse détaillée de quatre profils de vitesses mesurés sous couvert de glace. Ceux-ci sont comparés à un profil témoin, mesuré au même endroit, mais en l'absence de glace (été 2007). L'article présente des indices de la présence de structures macroturbulentes et discute de leur dynamique dans le contexte d'un écoulement caractérisé par deux CLT. L'article a été soumis à la revue *Water Resources Research*.
- 2) Le second article est intitulé *Cellules hélicoïdales dans un méandre de rivière en présence d'un couvert de glace* (traduction de l'auteur). L'article étudie la structure tridimensionnelle des écoulements à l'intérieur d'une section de rivière à méandre. Les résultats reposent sur une analyse spatiale du champ de vitesses de l'ensemble du méandre pendant les deux hivers successifs. L'effet du frazil sur le patron spatial des écoulements est brièvement abordé. L'article a été soumis et accepté dans le périodique *River Research and Applications* (sous presse).

## ***CHAPITRE I***

### ***MACROTURBULENT COHERENT STRUCTURES IN ICE-COVERED RIVER FLOW USING A PULSE-COHERENT ACOUSTIC DOPPLER PROFILER***

#### ***STRUCTURES MACROTURBULENTES MESURÉES À L'AIDE D'UN PROFILEUR ACOUSTIQUE À EFFET DOPPLER DANS UNE RIVIÈRE AVEC COUVERT DE GLACE***

##### Abstract

This paper presents the first field evidence of the presence of macroturbulent coherent structures in an ice covered river reach. Velocity profiles were obtained using a Pulse-Coherent Acoustic Doppler Profiler (PC-ADP) under an ice cover and are compared to measurements of open channel conditions. The results show that the friction imposed by the ice cover slows mean velocities at the water surface and results in a velocity profile with parabolic shapes of varying asymmetry. The Reynolds stresses in the streamwise ( $u$ ) and vertical ( $v$ ) components of the flow show positive values near the bed channel and negative values near the ice cover. The meeting point of the two boundary layers is a mean mixing layer dividing two types of coherent structure signatures, one pertaining to the ice cover and the other to the channel bed boundary layer. Using statistics applied to space-time matrices of flow velocities, vertically aligned stripes of coherent motions were revealed for both open channel and ice-covered flow conditions. In ice-covered conditions, they showed discontinued extensions with less frequent occupancy in proximity of the mixing layer. It follows that macroturbulence in ice-covered flow is highly reduced in scale when compared to open channel conditions: the streamwise length scale of the macroturbulent coherent structures is reduced from an average of 2.6 to 0.4 $Y$  ( $u$  component) and from 1.9 to 0.4 $Y$  ( $v$

component) where  $Y$  is the channel depth. The use of correlation matrices pairing time series of different flow depths was used to estimate the vertical extension of macroturbulent structures. During open channel conditions, the flow remains correlated over the entire flow depth, whereas in ice-covered conditions the mean extension was between  $0.58Y$  and  $1Y$  ( $u$  component) and  $0.81Y$  and  $1Y$  ( $v$  component). The reduced scale of macroturbulence is presumably associated with the roughness ratio between the ice cover and the bed channel at the reach scale. Each boundary wall generates its own set of macroturbulent motions that compete with each other in the outer region of the flow, enhancing mixing and promoting the dissipation of coherent structures. The apparent division of the flow is a dynamic frontier with overlapping coherent motions over both boundary layers, but these mixing phenomena tend to be very intermittent.

### Résumé

Des structures macroturbulentes sont mises en évidence dans une rivière en présence d'un couvert de glace. Des profils de vitesses mesurés sous couvert de glace à l'aide d'un profileur acoustique à effet Doppler sont comparés à un état de référence obtenu dans des conditions libres de glace. Les résultats montrent que la friction exercée par le couvert de glace retarde les écoulements de surface et se traduit par des profils de vitesses de formes paraboliques d'asymétrie variable. Les cisaillements de Reynolds dans la composante longitudinale ( $u$ ) et verticale au chenal ( $v$ ) de l'écoulement présentent des valeurs positives près du lit et négatives près du couvert de glace. Le point de rencontre entre les deux couches-limites est un plan de mélange entre des écoulements dominés respectivement par des signatures turbulentes propres au couvert de glace et au chenal. À l'aide de statistiques appliquées à des matrices spatio-temporelles de vitesses d'écoulement, des successions de structures macroturbulentes en bandes verticales sont révélées dans les écoulements. En condition englacée, ces macrostructures sont discontinues et moins fréquentes à proximité du plan de mélange. En conséquence, les structures macroturbulentes sont considérablement réduites en taille par rapport aux conditions libres de glace: la taille longitudinale des structures est réduite en moyenne de  $2.6$  à  $0.4Y$  (selon la composante longitudinale) et de  $1.9$  à  $0.4Y$  (selon la composante verticale) où  $Y$  est la profondeur de l'écoulement. L'utilisation de matrices de

corrélations appliquées aux vitesses de l'écoulement de profondeurs différentes permet de visualiser l'extension verticale des structures macroturbulentes. En période libre de glace, les vitesses sont corrélées sur toute la profondeur de l'écoulement alors qu'en période englacée l'extension varie entre 0.58 et  $1Y$  (composante longitudinale) et 0.81 et  $1Y$  (composante verticale). L'extension verticale est présument définie par le rapport de rugosité entre le couvert de glace et le lit du chenal à l'échelle du tronçon. Chaque plan de rugosité génère un groupe de structures macroturbulentes qui se propagent dans l'écoulement et qui se rencontrent au centre de l'écoulement, accentuant ainsi le mélange et la dissipation des structures cohérentes. Cette division n'est pas une frontière imperméable; en un point donné, des structures cohérentes peuvent survenir dans les deux couches-limites, mais ces incursions sont très intermittentes.

## ***1.1 Introduction***

In cold temperate climate, the winter season is associated with particular processes and interactions between the different components of fluvial systems (Allard *et al.*, 2009). Most notably, the formation of an ice cover has immediate and profound impacts on the flow structure of the turbulent boundary layer (TBL). Turbulent flow structure is a fundamental mechanism in the boundary layer that acts on mixing processes, sediment transport (Lapointe, 1992; Drake *et al.*, 1988; Cellino and Lemmin, 2004; Paiement-Paradis *et al.*, 2011), morphological change (Leeder, 1983; Best, 1993) and aquatic habitat (Davis and Barmuta, 1989; Carling, 1992). Central to the theme of turbulent flow structure is the occurrence of quasi-periodical coherent motions that promote strong exchanges between the inner and outer layers of the flow. The near-wall region, or inner layer, is a breeding ground for the production and self-sustainment of such coherent structures (Smith *et al.*, 1991; Smith, 1996). The main structures are the upward bursting of slow fluid motion called ejections and downward inrushes of fast fluid motion called sweeps (Kline *et al.*, 1967; Corino and Brodkey, 1969). These mechanisms contribute to most of the turbulence production (Kim *et al.*, 1971). Grass (1971) showed that these turbulent mechanisms are present in rough turbulent wall conditions and can be scaled with the size of the roughness elements (Grass, 1971; Grass *et al.* 1991; Defina, 1996; Grass and Mansour-Tehrani, 1996).

The outer layer of the flow was also found to present large coherent structures that scaled with the thickness of the boundary layer. These structures are hereby referred to as macroturbulent. The outer layer flow maintains correlated velocities throughout the boundary layer with signatures similar to those of ejections and sweeps (Brown and Thomas, 1977; Nakagawa and Nezu, 1981). Large bulges of coherent fluid motions were also found to occur coincidentally with alternating low and high-speed pulsations of flow compared to mean velocity (Falco, 1977). This macroturbulence was described as three-dimensional quasi-periodical vortices '*rolling*' in stable paths of the channel (Schvidchenko and Pender, 2001). Alternating pulses of high and low-speed velocities are equally present in both sand bedded (Levasseur, 1999) and gravel-bed channels (Ferguson and Kirkbride, 1995; Buffin-Bélanger *et al.*, 2000). Roy *et al.* (1996) found integral time and length scales to remain constant at

different flow depths, suggesting that the flow is dominated by coherent structures units occurring simultaneously over the entire flow depth. These large scale structures were found to have convex shaped fronts, forming wedges with a mean angle of  $36^\circ$  with the bed (Buffin-Bélanger *et al.*, 2000). Based on space-time correlation analysis applied to simultaneous velocity time series measured in various configurations of a gravel-bed river, Roy *et al.* (2004) presented the shape of wedges as elongated (3-5Y) and narrow features (0.5-1Y) where Y is flow depth. The mechanism that generates and sustains macroturbulent structures is still unclear (Robinson, 1991, Roy *et al.*, 2004; Nezu, 2005). Macroturbulent coherent flow structures occurring in the outer layer have been presented as the result of the coalescence of ejection motions expanding throughout the boundary layer (Head and Bandyopadhyay, 1981; Perry and Chong, 1982, Nezu and Nakagawa, 1993). Amalgamation of small-scaled coherent structures from eddy shedding and wake flapping in the lee of protruding particles could also set the conditions for larger scaled structures initiation in gravel-bed channels (Hardy *et al.*, 2009). Even if the inner layer is the main provider of turbulence production, studies have also shown that large scale structures occurring in the outer layer has a prominent influence on the inner layer turbulent processes (Roy and Blackwelder, 1994; Buffin-Bélanger *et al.* 2001).

To date, research addressing the hydraulic response to ice cover formation has focused mainly on the mean velocity profiles. Bulk flow velocity is slowed and depth correspondingly increased as a consequence of an additional roughness boundary in the perimeter of the flow (Ashton, 1986). Often, the ice undercover presents wavy forms similar to sand bedded ripples, effectively mimicking the roughness of a channel bed (Ashton and Kennedy, 1972). The general shape of the resulting velocity profile is a more or less symmetric parabolic form with peak velocities found toward the smoother boundary. In depth-limited flow typical of small rivers, the classical perspective is to consider the flow as two boundary layers that behave like two distinct open channel flows stacked on each other and meeting at the plane of maximal velocities. Logarithmic profiles can be applied independently to both velocity gradients leading to computerization of boundary parameters (Larsen, 1969). A few flume and field studies have also examined turbulent parameters in perspective of the two boundary layer hypothesis (Hanjalic and Launder, 1972; Parthasarathy

and Muste, 1996, Sukhodolov *et al.*, 1999). When applied piecewise to each boundary layer, profile trends of turbulence intensities and Reynolds shear stress are found to follow semi-theoretical predictions established for open channels. Close to the ice cover, Reynolds shear stress in the combined streamwise and vertical components of the flow show negative values. *Slow upward* and *fast downward* motions classically associated to coherent motions are turned upside down, leading to *slow downward* and *fast upward* motions. Thus, the plane where Reynolds shear stress crosses the 0-value can be viewed as a mean interface dividing two stacked boundary layers dominated by different turbulence signature, one pertaining to the ice cover and the other to the channel bed.

The assessment of macroturbulence dynamics in the case of a composite input of turbulence production is only tentative since no measurements were designed to focus at this scale of analysis. The aims of the paper are to identify macroturbulent coherent structures in an ice covered flow and to describe their geometry and spatial distribution in regard of the flow division in two TBL. The flow velocities are measured with a Pulse-Coherent Acoustic Doppler Profiler (PC-ADP), deployed in a small sand bedded channel with a fully developed ice cover. The PC-ADP is a non intrusive instrument that can measure profiles at a high vertical resolution simultaneously. It offers a unique opportunity to easily visualize and analyse in synchronicity the macroturbulent scale of turbulence over the entire flow depth without resorting to arrays of single point devices which would be delicate to deploy under an ice cover. The paper presents a series of analysis that follows the guidelines of classical techniques already used in the context of macroturbulence detection in open channel conditions (visualisation of velocity signals and correlation analyses) while fully exploiting the high density potential offered by the PC-ADP. The PC-ADP measurement technique and its potential in the measurement of turbulence parameters will first be reviewed since its use has yet to be widespread for the study of turbulence.

## 1.2 Methodology

### 1.2.1 Experimental design

A field survey was carried out in early March 2008 in a small meandering reach of the Neigette River, which is part of the catchment system of the Mitis River (Quebec, Canada). The river reach is deeply incised into cohesive clay deposits but the bed material is mainly composed of sand. Velocity profiles were collected at four locations at the upstream edge of a pool in a meander reach where the flow is nearly parallel to the banks and only mildly affected by centrifugal effect (figure 1.1a).

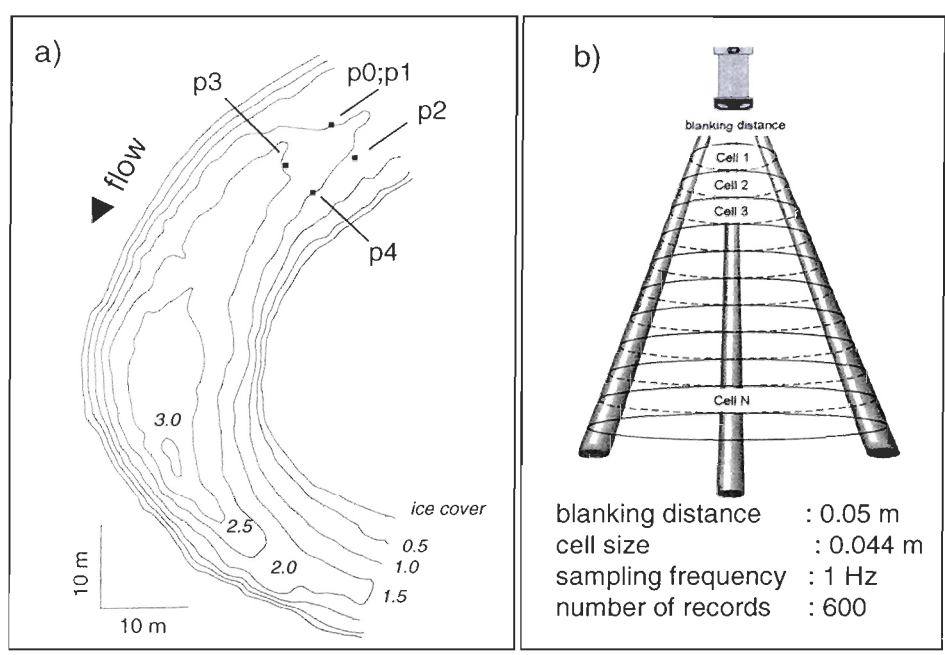
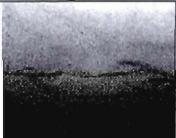
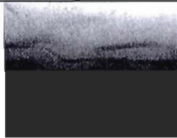
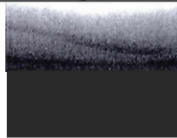


Figure 1.1: a) Sampling scheme in the Neigette River and b) setup parameters of the PC-ADP.

Four velocity profiles (p1-p4) were measured during ice-covered conditions. They are compared to one profile (p0) measured during open channel conditions (August, 2007). The latter profile was located at the same position as profile p1. At the time of the surveys, the discharges were estimated at 2.2 and 5.1 m<sup>3</sup>/s (~4% and ~10% of bankfull discharge) for winter and summer conditions respectively. It is recognized that the size of macroturbulent

coherent structures changes with flow depth and thus discharge. Incidentally, the results must be scaled with flow depth in order to measure the specific effect of the ice cover on macroturbulence dynamics. At each measurement station, the ice cover thickness was measured manually with a scaled rod and the ice undercover roughness was visually inspected using a submersible optical camera. Roughness was classified in three categories judging from the overall variability in the reach: smooth, smooth-rough and rough. The bed roughness was also visually inspected and was composed of uniform sand with localised ripples for all profile positions except p1 where a small woody debris was found to lay on the sand (diameter is  $\sim 2$  cm). Ice conditions and flow characteristics pertaining to each velocity profiles are summarized in table 1.1. Change in flow depths and velocities along with ice cover thickness and roughness variability offer a wide range of conditions.

Table 1.1 : Physical characteristics at velocity profiles sampling location

Profile #	p0	p1	p2	p3	p4
Undercover roughness	No ice cover	 rough	 rough	 smooth-rough	 smooth-rough
Ice cover thickness (m)	-	0.61	0.55	0.61	0.60
Flow depth (m)	1.30	1.08	0.86	1.66	1.04
Mean velocity (m/s)	0.38	0.35	0.18	0.25	0.12

Velocity data were collected using a *Sontek* 1.5Mhz Pulse Coherent Acoustic Doppler Profiler (PC-ADP). This instrument measures simultaneous velocities over the entire flow depth and in all three components of the flow (longitudinal, vertical and lateral). The PC-ADP relies on a particular measurement technique, the coherent mode, which can reach vertical resolutions as low as a few centimetres (Lhermitte and Serafin, 1984). The device sends two short sound impulses in the water column where it is backscattered by the buoyant particles in movement with the water (pings). The phase shift ( $\Delta\Phi$ ) between the two signals is related to the particles velocity ( $V_p$ ) by the relation:

$$V_p = \frac{c\Delta\Phi}{4\pi F\Delta t} \quad (1)$$

where  $c$  is the speed of sound in water,  $F$  is the signal frequency of the instrument and  $\Delta t$  is the time lag between the two sound impulses (Lacy and Sherwood, 2004). Each ping is listened and measured at different time lags leading to estimation of flow velocities at several flow depths from the instrument. Multiple pings are then averaged over a user defined sampling frequency that can reach a maximum of 2 Hz. Velocities are measured parallel to three radial beams inclined with a  $15^\circ$  with the axis of the instrument, forming a sampling volume extending outward in the water in the shape of a cone (figure 1.1b). Measurements are made through *cells* which correspond to horizontal slices of the cone. Along beam velocities are afterward converted into a cartesian framework which assumes that flow measured by all beams is equivalent. This means that flow must be homogeneous in the sampling volume determined by the perimeter of the beams and the vertical length of the cells. Non-homogeneity can be encountered in highly turbulent flow and in complex three dimensional flow fields, especially when it is coupled with a large sampling volume located far from the instrument. We used a tripod mount with a scaled rod which allowed us to insert the instrument head even with the ice undercover. Ice covered mounting setup reduces flow disturbance normally caused by instrument intrusion in the water, so the blanking distance, the no-see area near the nose of the instrument, was set to its minimum length of 0.05 m. Every profile was measured at a constant vertical resolution of 0.044 m and at a sampling frequency of 1 Hz for time series of 10 minutes (600 records).

### 1.2.2. Data validation

Along with the velocity data, the PC-ADP measures quality parameters, the signal to noise ratio (SNR) and correlation values that help to evaluate the reliability of sampled data (Sontek, 2004). The SNR is a measure of sound intensity compared to background noise and is linked to the presence of sufficient particles in the water to properly reflect back the signal to the instrument. Sontek (2004) recommends a minimum of 5 db and this criterion was constantly met in all time series collected (mean SNR is 21.7 db with a standard deviation of

2.6). The correlation values are a measure of coherency between each sound impulses pair and are linked to many sources of errors among which lack of flow homogeneity within the sampling volume is a predominant factor. No minimal limit is recommended since correlation value is also function of environmental conditions, mainly determined by intensity of turbulence mixing. Mean correlation value is 0.43 for the profile during open channel conditions (standard deviation is 0.071) and 0.13 for all other ice covered profiles (standard deviation is 0.027). Thus, the ice cover is found to diminish correlation values, perhaps because of increased sound interferences or lesser flow homogeneity. Time series were removed when correlation values showed a decrease of two standard deviations from the profile mean correlation. In figure 1.2, black horizontal stripes show the cells that have been removed. They are almost systematically located close to the bed (except one for profile p4). This is because sound interference and bed non uniformity typically hinders the capacity of the PC-ADP to resolve the cells nearest to the bed.

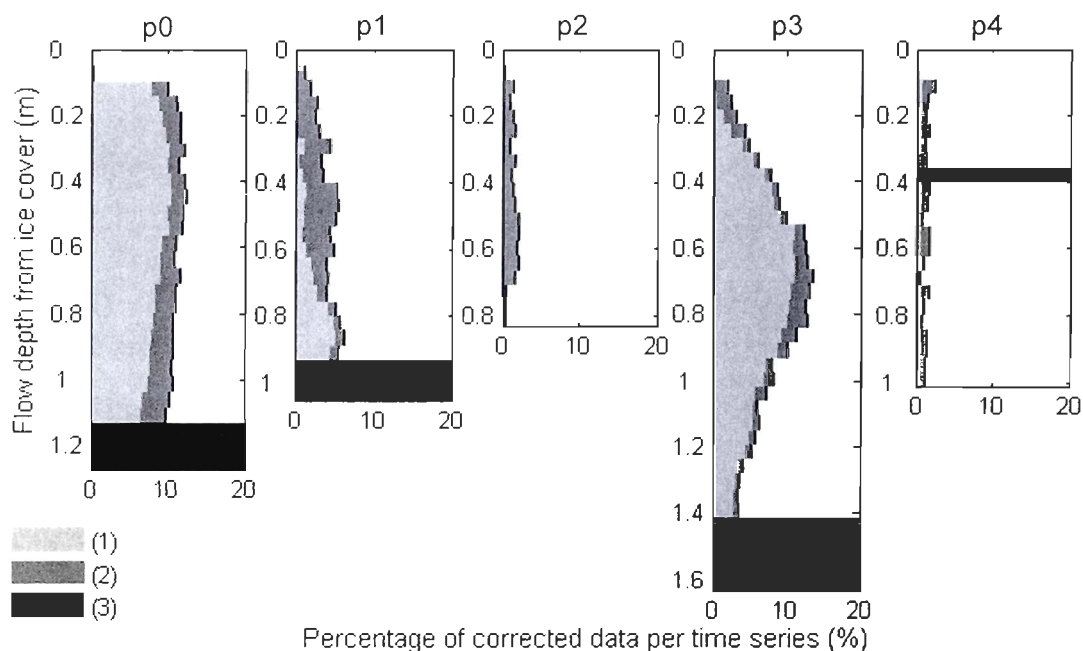


Figure 1.2 : Percentage of data corrected per time series using (1) the algorithm of ambiguity correction (light gray) and (2) the de-spiking algorithm (dark gray). Black stripes (3) identify time series entirely removed.

One specificity in the use of an ADCP in coherent mode is the constant tradeoff between the profiling range ( $p_{\max}$ ) and the maximum velocities resolvable (Lhermitte and Serafin, 1984,

Lohrmann *et al.*, 1990). Measurement of the phase shift between two successive impulses is theoretically limited to an extent of  $2\pi$  ( $360^\circ$ ). This limit corresponds to a velocity that is called the ambiguity velocity ( $V_A$ ) and can be linked to the profiling range ( $p_{\max}$ ) by the relation:

$$V_A = \frac{c^2}{4Fp_{\max}} \quad (2)$$

Thus, maximum resolvable velocities are inversely related to the profiling range. Velocities higher than  $V_A$  will result in data corruption called ambiguity error that implies that the true velocity is underestimated by a factor of  $V_A$ . This problem can be limited by minimizing the time between the two sound impulses ( $\Delta t$ ) which shortens the phase shift observed, thus keeping velocity measurements under the maximum limit. However, a short time lag also reduces the time allowed to receive the backscattered sound impulses, limiting the maximum profiling range ( $p_{\max}$ ). The *Sontek* PC-ADP addresses this tradeoff problem by using an independent velocity measurement made at a *resolution cell* fixed at a shorter profiling range ( $p_{\text{res}} \ll p_{\max}$ ) thus ensuring a maximum resolvable velocity range for this specific measurement. If accurate, this velocity can later be compared to velocity data collected over the entire profiling range set by the user ( $p_{\max}$ ). We used the algorithms of Lacy and Sherwood (2004) as modified by Cassista (2007) based on this independent velocity to resolve every other measurement. Their approach is twofold, including 1) the treatment of the velocities measured in the resolution cell and 2) the comparison of this measure with every other data collected:

1. The spikes in the velocity time series of the resolution cell are first removed with the use of Goring and Nikora (2002) filter algorithm. When correlation values of the resolution cell is less than 25%, the detection threshold of spikes is reduced by a factor of 0.3. Afterward, the time series are smoothed with a Butterworth filter with a cutoff frequency of 30 seconds.
2. For each profile, velocities measured in the resolution cells are compared with the values in the profile cell located closest to it. If the difference between the two data is more than  $0.5V_A$ , the velocity is adjusted by adding  $V_A$ . This corrected (or not) velocity is then compared with every other cells, first upward and secondly downward the profile. Every

time the difference is more than  $0.5V_A$ , the data is corrected by adding  $V_A$ . After the examination of the vertical profiles, adjacent values of individual time series are compared with each other, each time using the same correction when the difference is higher than  $0.5V_A$ .

In figure 1.2, light gray bars show the proportion of velocity measurements per time series that were corrected by the algorithm for the correction of ambiguity errors. Profiles p0, p1 and p3 present the highest amount of ambiguity correction. As expected, these profiles correspond to the deepest and fastest flow (table 1.1). The distribution of ambiguity correction along individual profiles also closely follows the trends of expected mean velocity profiles. Visual inspection of time series showed that the algorithm was unable to remove all aberrant data. Hence, the algorithm of Goring and Nikora (2002) for de-spiking time series was also applied a second time to adjust these measurements. This approach is unlike the resolution of ambiguity errors. The data are not replaced by  $V_A$ , but by a probable value determined by its neighbours. In figure 1.2, dark gray bars show the percentage of measurements per time series that were adjusted by this second algorithm. The amount of corrected values is fairly constant over flow depth and follows no systematic trend. In some occasions, the de-spiking affected time series that were left unchanged by the ambiguity error correction. It is likely that the de-spiking algorithm affected both ambiguity errors and a certain amount of valid velocity measurements. Considering the low amount of corrected data (~2%), this solution has nonetheless proved to efficiently remove the last ambiguity errors as assessed by a visual examination.

### *1.2.3. Data analyses*

Table 1.2 presents the conclusions from studies that have compared flow parameters measured by the PC-ADP with those measured by an Acoustic Doppler Velocimeter (ADV), a device commonly used in the study of turbulence (Voulgaris and Trowbridge, 1998; Lane *et al.*, 1998). Considering a spatial framework where  $x$ ,  $y$  and  $z$  respectively represent the streamwise, normal and spanwise axis of the flow, the corresponding velocity components of

the flow are defined as  $u$ ,  $v$  and  $w$ . Each component can be divided into its mean ( $\bar{u}$ ,  $\bar{v}$ ,  $\bar{w}$ ) and fluctuating parts ( $u'$ ,  $v'$ ,  $w'$ ). The intensity of this fluctuating part is expressed by the standard deviations of the time series, quoted as  $s_u$ ,  $s_v$  and  $s_w$ . Finally, the covariance between the  $u$  and  $v$  components of the flow, the Reynolds stresses ( $-\overline{\rho u'v'}$ ), is also considered because of its significance for turbulent exchanges of momentum and its relevance in documenting coherent structures occurrence and dynamics. As shown in table 1.2, mean flow estimated by the PC-ADP are reliable parameters that present only small deviations when compared to ADV measurements. However, this consistency between the two devices does not hold for standard deviations estimations. When flow is not completely homogeneous, transformation from beam velocities to a cartesian framework introduces variance in the longitudinal and lateral components and reduces variance in the vertical components when compared to ADV measurements. This is because the noise measured in the beam axis is transferred with different magnitudes to the different flow components of the cartesian framework depending on the angle proximity between the two (Hurther and Lemmin, 2001). Because of the variable incidence of geometry transformation on the different flow components, Reynolds stresses are underestimated when pairing either longitudinal or lateral components with the vertical component of the flow. However, the vertical profiles of the turbulent variables tend to follow theoretically expected trends (Muste *et al.*, 2004; Cassista, 2007; Nystrom *et al.*, 2007).

Table 1.2: Correspondences of mean and turbulent parameters as measured by the PC-ADP when compared to the ADV

Flow parameters	Tilston and Biron (2006)	Cassista (2007)	Nystrom <i>et al.</i> (2007)
$\bar{u}$	▲	≡ (3%)	≡ (2%)
$\bar{v}$	≡	≡	n/a
$\bar{w}$	▼	≡	n/a
$s_u$	▲	▲ (60%)	n/a
$s_v$	▼	▼ (40%)	n/a
$s_w$	▲	▲ (100%)	n/a
$-\overline{\rho u'v'}$	n/a	▼	▼ (90%)

≡ : equivalency, ▲ : overestimation of the PC-ADP, ▼ : underestimation of the PC-ADP, n/a : not available, (\*) magnitude of difference if available

The capacity of the PC-ADP to accurately estimate other turbulent variables has not reached a consensus so far. This paper makes use of visualization techniques applied to time series as well as various correlation techniques that could be affected by the larger spatial sampling volume of the PC-ADP. The results will thus be consistently examined for possible bias and the interpretation will remain prudent. A classical technique used for the visual detection of large scale flow structures from velocimetric data relies on individual time series analysis using standard deviations as thresholds to identify high or low-speed deviance from the mean flow (Falco, 1977; Buffin-Bélanger *et al.*, 2000; Roy *et al.*, 2004). Initial results from this technique yields good results for open channel conditions, but the higher complexity of the flow in ice-covered conditions was poorly characterized using this approach (unpublished results). Figure 1.3a illustrates the initial  $u$ -velocities of profile p0 (open channel conditions). Velocity signals (shades of gray) are presented in stacked cells representing flow fluctuations from the bed (bottom) to the surface (top) of the channel. Figure 1.3b shows the conversion of the initial time series in a binary representation of low (white) and high-speed (black) flow compared to the cells mean velocities. This yields a streaky structure that covers various time lengths. Nystrom (2001) described the most ephemeral streaky structures as the result of the temporal averaging of the PC-ADP. One solution to effectively remove these artefacts would be to further specify deviances from the mean with standard deviations units to keep considering only the largest scales of turbulence. The high density of data measured by the PC-ADP offers the opportunity to use alternative techniques that also considers the vertical continuity in the data. Anselin's algorithm for local indications of spatial associations (LISA) is a statistical test which locally identifies the presence of positive and negative autocorrelation in a spatially distributed phenomenon (Anselin, 1995). The longitudinal (individual time series) and vertical continuity (between measurement cells) in flow fluctuations can thus be equally considered on a simple proximity basis. For each observation, the algorithm computes an index that measures the auto-similarity or dissimilarity with a set of adjacent observations located inside a predefined space window. For each observation, the index  $I_i$  is computed with the formula:

$$I_i = z_i \sum_j w_{ij} z_j \quad \text{for } j \neq i \quad (3)$$

where the subscript  $i$  represents the observation for which the index is to be calculated, the subscript  $j$  is all other measurements in the predefined window,  $z$  is the standardized values and  $w$  is a weight that represents the spatial relationship between all pairs of  $i$  and  $j$ . For randomly sampled values,  $I_i$  follows a normal curve distribution. When  $z$ -score values are lower than  $-1.96$  or higher than  $1.96$ , the null hypothesis (no autocorrelation) can be rejected with an alpha error of  $0.05$ . A positive significant value indicates local similarity in the data while a negative value indicates local dissimilarity. This type of analysis was initially designed for spatial data, but it can also be used for data where space can be substituted by time. In the context of flow velocity measurements, positive autocorrelations can be interpreted as local clusters of coherent motions amid a more complex ambient flow. The LISA algorithm is dependent on the size window as well as the weight that defines the spatial relationship between the observations. Preliminary analyses indicated that a growing window size produces larger local associations. The algorithm was applied to data sharing a direct neighbourhood with each other in the matrix with weights equally distributed in all directions, including oblique neighbourhood ( $9 \times 9$  matrices). This implicitly assumes some anisotropy in the results favouring the vertical connectivity since the cells are spatially closer ( $\sim 4.4$  cm) from each other than successive measurements in time (real distance is function of mean velocity). Prior to the application of the algorithm, each time series was standardized. This was to effectively group the data on the basis of its deviation from the local mean and to discard the influence of the shape of the velocity profile. Figure 1.3c shows the result of the LISA algorithm. Black and white cells respectively represent significant clusters of higher and lower velocity compared to the cell mean velocities. When compared to the upper graphs, the visual effect of figure 1.3c is to remove the noise of variations that do not present space-time coherency, hence by-passing small-scaled streaky structures possibly yielded by temporal averaging.

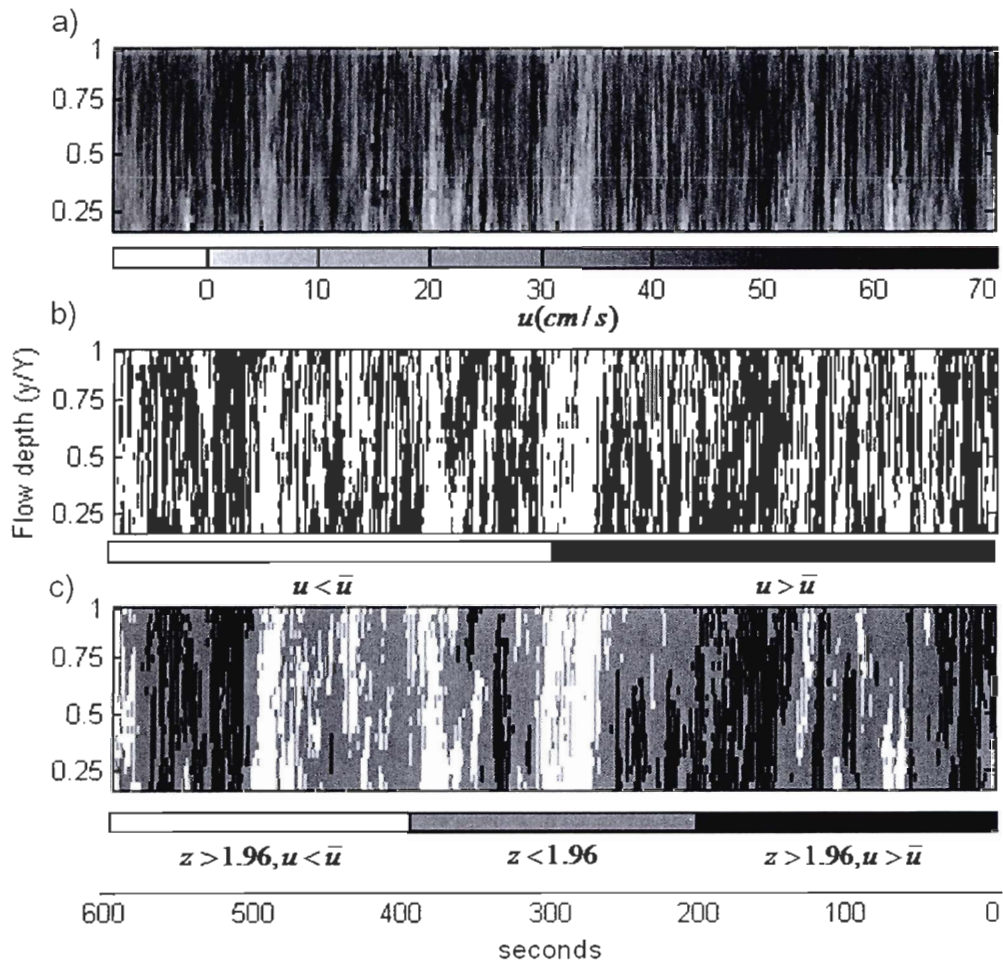


Figure 1.3: a) Velocity time series as collected by the PC-ADP after data validation, b) binary representation of the velocities from their deviance from the mean and c) identification of clusters of coherent motions in the flow from the LISA algorithm. To represent the flow as if it is moving from left to right, the time series are plotted from the end to the beginning of the actual time in data collection.

Various correlation techniques are used to assess the scale of macroturbulence and its spatial organization. Space-time correlations were applied between all measured cells of the PC-ADP. Correlation coefficients ( $r$ ) are computed between two different time series ( $u_1$  and  $u_2$ ) while considering an array of temporal lags ( $\Delta t$ ) between the two. Correlation coefficients are computed from:

$$c_{u_1 u_2}(\Delta t) = \sum_{i=1}^{N-\Delta t} (u_{1i} - \bar{u}_1)(u_{2i+\Delta t} - \bar{u}_2), \text{ for } \Delta t \geq 0 \quad (4)$$

$$c_{u_1 u_2}(\Delta t) = \sum_{i=1-\Delta t}^N (u_{1i} - \bar{u}_1)(u_{2i+\Delta t} - \bar{u}_2), \text{ for } \Delta t < 0 \quad (5)$$

and

$$r_{u_1-u_2}(\Delta t) = \frac{c_{u_1 u_2}(\Delta t)}{s_{u_1} s_{u_2}} \quad (6)$$

where  $u_i$ ,  $\bar{u}$ ,  $s_u$  and  $N$  are respectively the instantaneous velocity, the average velocity, the standard deviation and the number of measurements of the time series  $u_1$  and  $u_2$  and where  $c_{u_1 u_2}$  is the covariance between the two. The similarity of successive measurements in each time series is also measured using autocorrelation functions (ACF). In ACF, correlation coefficients ( $r$ ) are computed for individual time series at different time lags using  $u_1$  in place of  $u_2$  in equation (4) and (6). The integral time scale is the time lag until correlation coefficients first underscores the threshold for statistical significance ( $\alpha = 0.05$ ). When multiplied by  $\bar{u}$ , ITS values can be converted to Integral Length Scales (ILS), which is a measure of the mean length of coherent structures. This analysis postulates that Taylor's hypothesis of frozen turbulence is valid and can be converted into a distance scale when the flow is not modified by significant shear (Taylor, 1935).

### 1.3. Results

#### 1.3.1. Mean and turbulent parameters

Figure 1.4a shows the streamwise velocity profiles measured by the PC-ADP for both open (p0) and ice-covered flow conditions (p1; p2; p3; p4). As expected for depth-limited open channel flows, p0 presents a gradual velocity gradient typical of a single boundary layer occupying the entire flow depth. The effect of the ice cover on the vertical distribution of streamwise velocities is revealed on the other four profiles by an inverse velocity gradient near the water surface. The two boundary layers meet in the outer region where maximum velocities are found. The dimensionless depths representing the plane of maximum velocities ( $y_{\text{umax}}/Y$ ) dividing the two boundary layers are presented in table 1.3. Three out of four ice covered profiles (p2; p3; p4) have clearly defined points of maximum velocities. However,

p1 has a flat velocity profile that makes difficult to define the exact location of the maximum velocity.

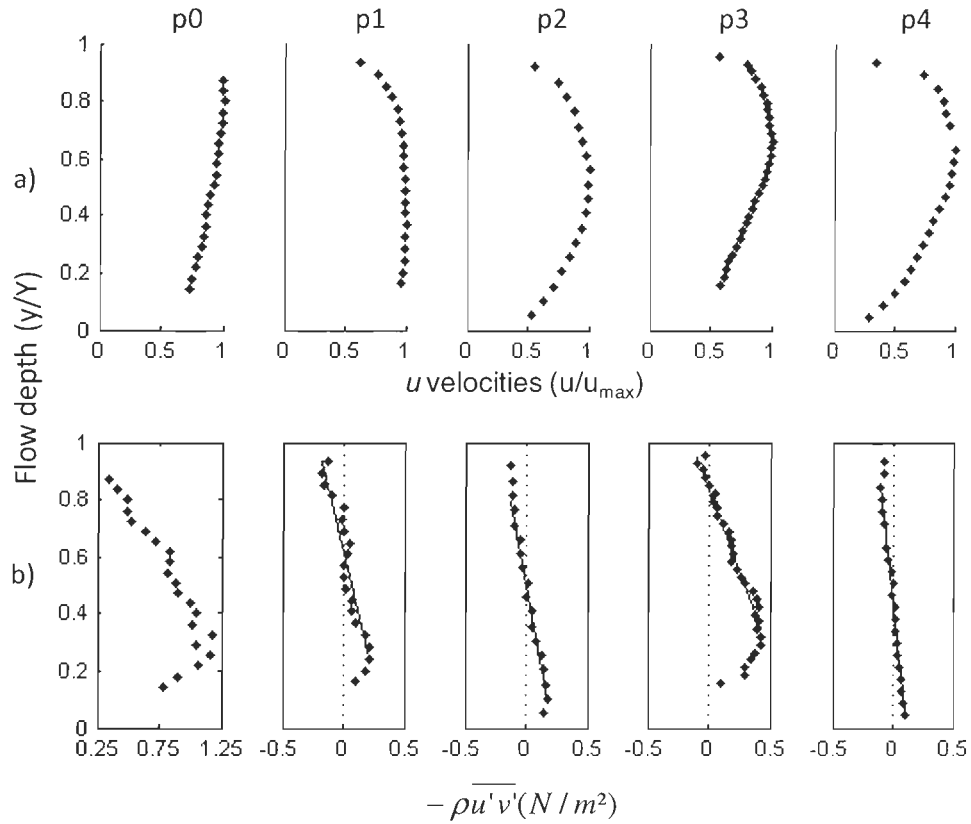


Figure 1.4: a) Velocity profiles and b) Reynolds shear stress for profiles measured during open (p0) and ice-covered flow conditions (p1; p2; p3; p4). Note the different range of values for profile p0.

Table 1.3: Dimensionless depths of the plane of maximal velocities ( $y_{u_{max}}/Y$ ) and zero Reynolds shear stress ( $y_{uv=0}/Y$ )

	P1	P2	P3	P4
$y_{u_{max}}/Y$	0.37*	0.66	0.56	0.63
$y_{uv=0}/Y$	0.61*	0.52	0.84	0.44
$r^2$ of LSR	0.86	0.98	0.98	0.98
slope of LSR	-1.74	-2.25	-1.15	-3.8

\*exact location is unclear

Figure 1.4b shows the vertical distribution of Reynolds shear stress values ( $-\overline{\rho u'v'}$ ). In open channel conditions, Reynolds shear stress increases from the channel bed until  $0.3Y$  where it peaks at  $1.18 \text{ N/m}^2$ . Above, it decreases near null values at the water surface. In ice-covered flow conditions, Reynolds stress values are positive in the region close to the bed and negative in the region affected by ice. Two types of profile shapes are apparent. Profiles p2 and p4 have linear trends while profiles p1 and p3 have more sinuous trends with  $S$ -shaped forms. The outer region trends allow the identification of the horizon where  $-\overline{\rho u'v'} = 0$  with standard least square regressions (LSR). The models have been applied to all values between the most negative and positive values of the profile to avoid the scatter along the  $S$ -shaped trends. Results of dimensionless flow depths values for the plane of zero shear stress ( $y_{uv=0}/Y$ ) are presented in table 1.3. Profile p1 has the peculiarity to present a flat front in the outer region that sticks more or less to the 0-value. The standard least square procedure identifies a precise transition that, in fact, covers a wider range of depth values (from  $\sim 0.5Y$  to  $\sim 0.75Y$ ). The trend of profile p3 is almost restricted to the upper half of the profile and crosses the plane of zero shear stress only very close to the ice cover. This shape is strikingly similar to the one measured during summer conditions (p0). For all ice-covered profiles, the range of Reynolds shear stress values is similar, varying between  $-0.18$  and  $0.21 \text{ N/m}^2$ , with the exception of p3 where values reach a maximum of  $0.43 \text{ N/m}^2$ . In all cases, Reynolds shear stress values in ice-covered flow conditions are much lower than in open channel flow conditions (ranging between  $0.34$  and  $1.18 \text{ N/m}^2$ ).

### *1.3.2. Visualization of macroturbulent coherent flow structures*

Figures 1.5 and 1.6 present the space-time velocity matrix used in the LISA algorithm as well as the proportion of time when clusters are identified as lower or higher than mean velocities. In open channel conditions, velocity fluctuations for both the  $u$  and  $v$  components show well defined stripes of vertically organized clusters covering a proportion of the flow depth, sometimes occupying the entire water column. For the  $u$  component of flow, identified clusters correspond to 40.7 % of all data and equally include higher and lower than average zones. Also, the frequencies show that clusters are evenly represented along the vertical

profile. They often slightly diverge from perfect verticality, but definite obliquity trends are not obvious. For the  $v$  velocity component, identified clusters represent 28.9% of all data. Clusters also tend to organize in vertical stripes, but have shorter time lengths and tend to be slightly more frequent in the core area of the profile. For both components of the flow, no clear succession of lower and higher than average velocities can be readily observed.

In comparison, the ice-covered flow velocity profiles seem disorganized. For the  $u$  component of flow, clustered velocities represent 13% (p1), 21.8% (p2), 21.9% (p3) and 23% (p4) of all data compared to 40.7% for open channel conditions. Clusters appear also vertically aligned and can cover a significant proportion of the flow depth. However, the frequency distribution shows that clusters are more frequent toward the boundaries and less frequent at mid-depths of flow, with a definite asymmetry favouring cluster occurrence near the bed channel rather than the ice cover. The position of lowest frequencies appears to occur very close to the interface of  $y_{uv=0}/Y$ . For a better visual interpretation of this relation, this interface is presented by a dot line on each graph. In cases where the interface is not systematically coincident with the very lowest values of frequencies, it appears nonetheless close to a zone of decreasing frequency values for profiles p1, p2 and p3. Also, the more pronounced is the gradient of Reynolds shear stress values, the clearer is the decrease in cluster frequencies (see table 1.3 for gradient values). Profile p1 has no variations of Reynolds stresses in the mid region of the flow and this is reflected by a mild variation in the frequency of the clusters. Profile p3 has the most pronounced gradient of Reynolds shear stress values over depth and this is reflected by a large variability of frequencies over depth. A close examination of individual clusters reveals that they can occasionally interpenetrate both boundary layers. However, on average, clusters are lengthier and more frequent near the boundaries and shorter as they reach and cross the interface of  $y_{uv=0}/Y$ . Coherency is also better defined near the channel bed, reflecting the asymmetry in boundary roughness and its influence in the production of turbulent coherent motions.

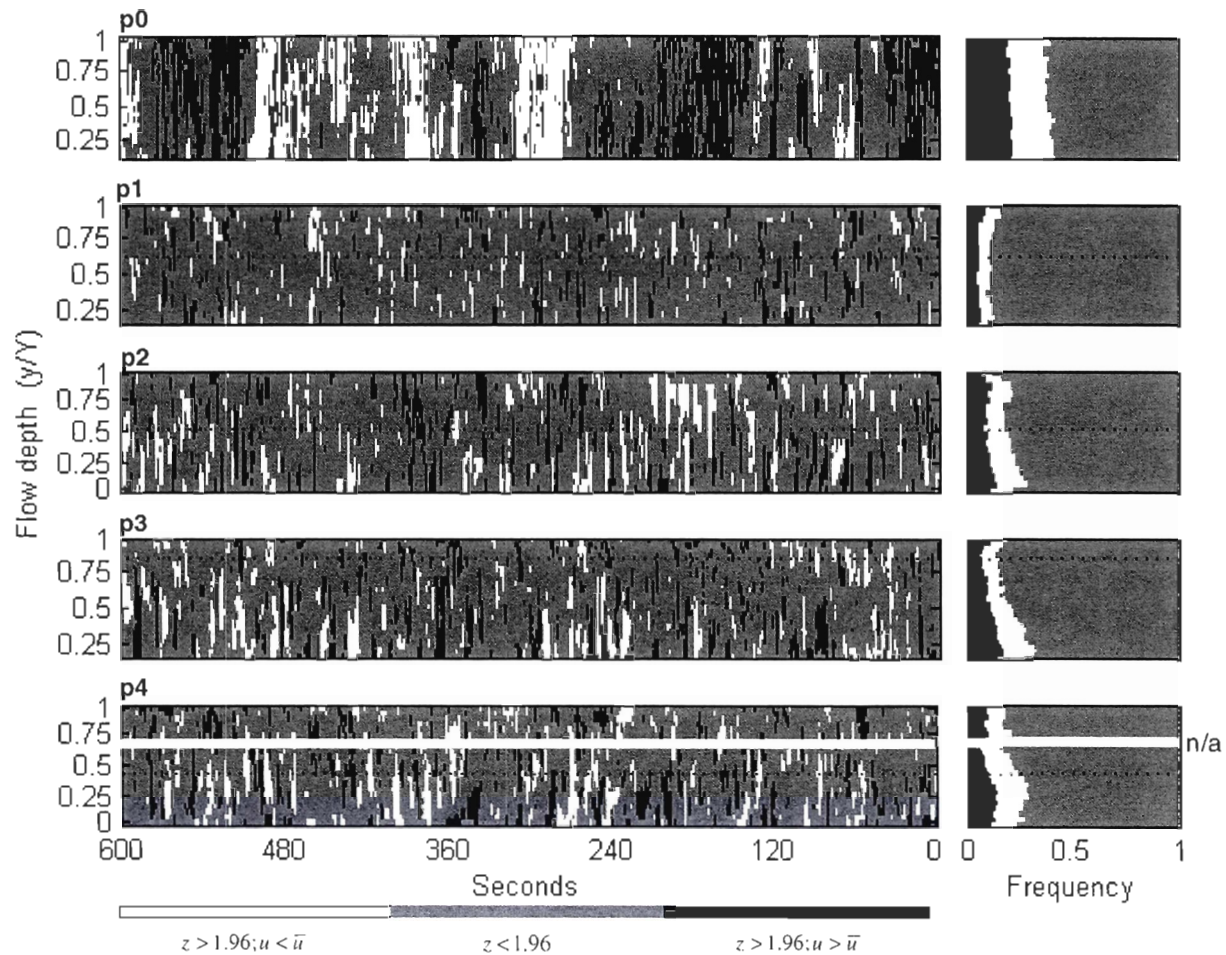


Figure 1.5: Clusters of coherent motions as revealed by the LISA algorithm when applied to the  $u$  component of the flow. Data with lower and higher than local average velocities are respectively presented as white and black cells. On the right hand of each profile, a frequency diagram illustrates how often cell velocities have been grouped in a given cluster type. The dot line is  $y_{uv=0}/Y$ .

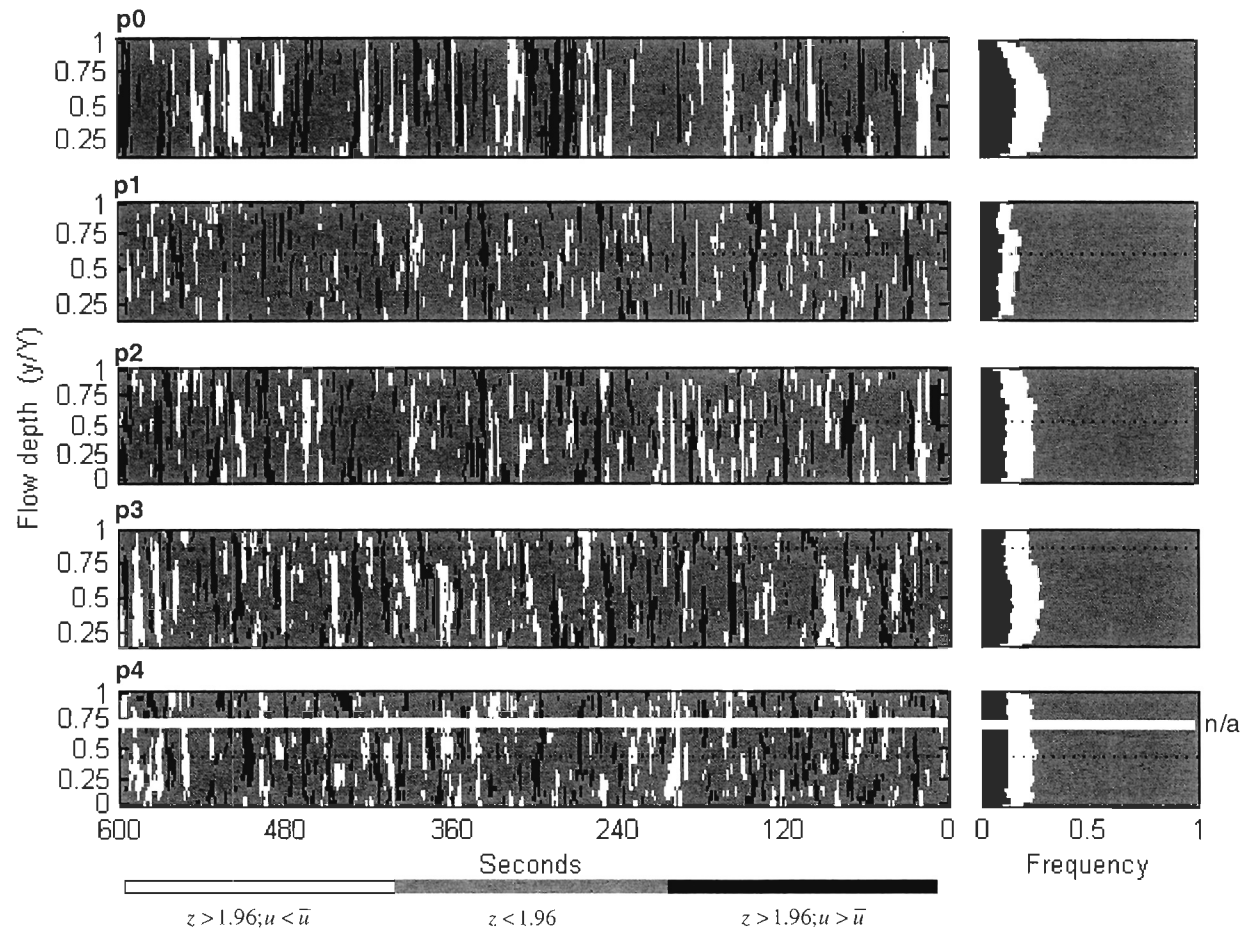


Figure 1.6: Clusters of coherent motions as revealed by the LISA algorithm when applied to the  $v$  component of the flow (refer to figure 1.5 for extended caption description).

The  $v$  component of flow presents a different pattern. Clusters represent 17.6% (p1), 24.3% (p2), 26% (p3) and 24.6% (p4) of total data, a proportion that is systematically higher than for the  $u$  component. This increased frequency appears to be more evenly distributed along the water column with perhaps a meagre peak somewhere in the profile, though without any obvious pattern in its location. No relation with the interface  $y_{u=v=0}/Y$  can be seen. This does not imply that individual clusters cover the entire flow depth. When looking more specifically at individual clusters, it is obvious that their vertical extension is limited, but they occur everywhere in the profile.

### *1.3.3. Integral time and length scales of macroturbulence*

Figure 1.7 presents values of Integral Time Scales (ITS) and Integral Length Scales (ILS) for the  $u$  and  $v$  velocity component. The  $ITS_u$  and  $ILS_u$  values of the open channel profile range respectively between 7-11 seconds and 2.5-4.5 meters. The  $ITS_u$  values have no visible vertical trend, generally remaining constant over the depth of flow, while  $ILS_u$  values closely follows the gradient of the mean velocities of the profile. The mean  $ILS_u$  value over depth is 3.4 meters and corresponds to 2.6 times the flow depth. The  $ITS_v$  and  $ILS_v$  values range respectively between 3-11 seconds and 1.1-3.8 meters. Mean  $ILS_v$  equals to 2.5 meters and corresponds to 1.9 times the flow depth. Here, a definite trend of increasing values toward the bed is apparent for both variables.

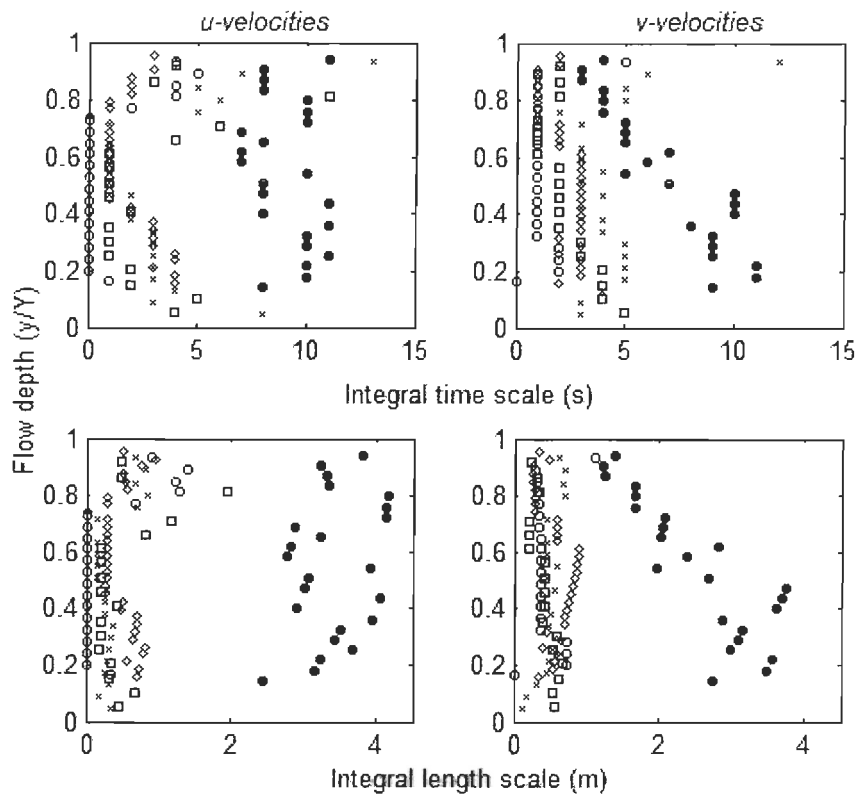


Figure 1.7: Integral time scales (ITS) and integral length scale (ILS) of open channel and ice covered flow conditions for the  $u$  and  $v$  components of the flow.  $p_0 = \bullet$ ;  $p_1 = \circ$ ;  $p_2 = \square$ ;  $p_3 = \diamond$ ;  $p_4 = \times$ .

Integral time and length scales of macroturbulence for ice-covered profiles have drastically different features. For the  $u$  component,  $ITS_u$  and  $ILS_u$  values respectively range between 0-6 seconds and 0-1.5 meters. The mean length scale of all four profiles averages 0.4 meter, corresponding to 0.38 of the flow depth. This central value varies along the depth of flow in a crescent shape trend with maximum values in the vicinity of the ice and bed boundaries and lower values in the outer region of the flow. For the  $v$  component,  $ITS_v$  and  $ILS_v$  values respectively range between 0-1.5 seconds and 0-1 meter. Mean  $ILS_v$  value is 0.48 and corresponds to 0.42 times the flow depth. The crescent shape observed for the  $u$  component can still be observed for the  $ITS_v$  values, but is very subtle for the integral length scale. The results of ITS and ILS values for the  $u$  component are consistent with the results from the LISA analysis. For open channel conditions, the autocorrelation function reveals that flow

coherency over time is constant regardless of flow depth. For ice-covered conditions, the crescent shaped patterns along the ITS and ILS profile values follow the same pattern revealed by the LISA algorithm where clusters of coherent motions were more present near the boundaries and less frequent towards the interface of zero Reynolds stresses. If the pattern between the ACF and the LISA analysis are consistent, the time persistency and, consequently, the length scales of coherency are not. The LISA algorithm presented the clusters as very large and intermittent. However, the length of clusters identified with the LISA algorithm is dependant upon the space window and the weight parameters. The ACF yields a true length scale of macroturbulence structure.

#### 1.3.4. Inclination of macroturbulent structures

Following Buffin-Bélanger *et al.* (2000), angles of inclination to the channel bed of large scale turbulent structures ( $\varphi$ ) can be estimated for each pair of cells in the vertical profile from:

$$\tan(\varphi) = d / (L_{\max} * \bar{u}) \quad (7)$$

where  $d$  is the vertical distance between two cells,  $L_{\max}$  is the time lag of maximum cross-correlation between the two cells and  $\bar{u}$  is the mean velocity of the top cell. The small sampling frequency (1 Hz) limits the capacity to detect the presence of weak inclinations. If one accepts a mean inclination of  $36^\circ$  for large scale turbulent structures as reported in gravel-bed rivers (Buffin-Bélanger *et al.*, 2000), uses an average flow velocity of  $\sim 40$  cm/s and a minimum time lag of 1Hz, the vertical distance between the cells needed to detect an inclination would be  $\sim 30$  cm. So, time series sufficiently distant from each other could in theory allow to estimate an angle of inclination. For each profile, cross-correlation analyses were computed considering a range of time lags of  $\pm 5$  seconds between two time series. Cross-correlations were applied between a fixed cell, the third from the ice cover, and every downward cell of the profile. The third cell was chosen instead of the first or second because

of the small proportion of significant correlation values for the first two cells with the other cells of the profile.

Figure 1.8 presents the results of cross-correlation values in the form of isolines for both open channel and ice covered conditions. In open channel conditions, correlation values show a constant decrease with distance, although all cells remain significantly correlated over the flow depth. Maximum values remain centered on the 0-lag line suggesting that the flow structures tend to follow a near vertical axis, which is consistent with the LISA analysis (figure 1.5). Considering the range of depths covered from the third top cell to the last bottom cell (1.03 m) with no time lag trends detected in the cross-correlation, it follows that the inclination with the bed of the structures would be superior to  $68^\circ$ . This is far higher than angles previously reported for gravel-bed rivers, but agrees with the shape of the clusters observed in the time series (figure 1.5 and 1.6). Clearly, a higher sampling frequency is necessary to further assess the exact obliquity of large scale turbulent flow structures in sand bedded channels. In ice-covered conditions, cross-correlations values decrease with distance, but at a faster rate than in open channel conditions. For profiles p1, p2 and p3, correlation coefficients are not significant at flow depths of 40 to 50 cm under the ice cover. In profile p3, higher correlation values reappear further down the profile until a depth of  $\sim 1.25$  m. In p4, correlation values remain statistically significant over the entire flow depth at lag times of 0. For all profiles, there appears to be no systematic shift in the lag of maximum correlation values, as it is centered on lag = 0. However, there also appears to be an asymmetry in correlation values between positive lags (backward flow) and negative lags (forward flow), favouring the latter (more pronounced for the 0.06 and 0.2 isolines). This asymmetry suggests a possible slight forward inclination starting from the ice cover.

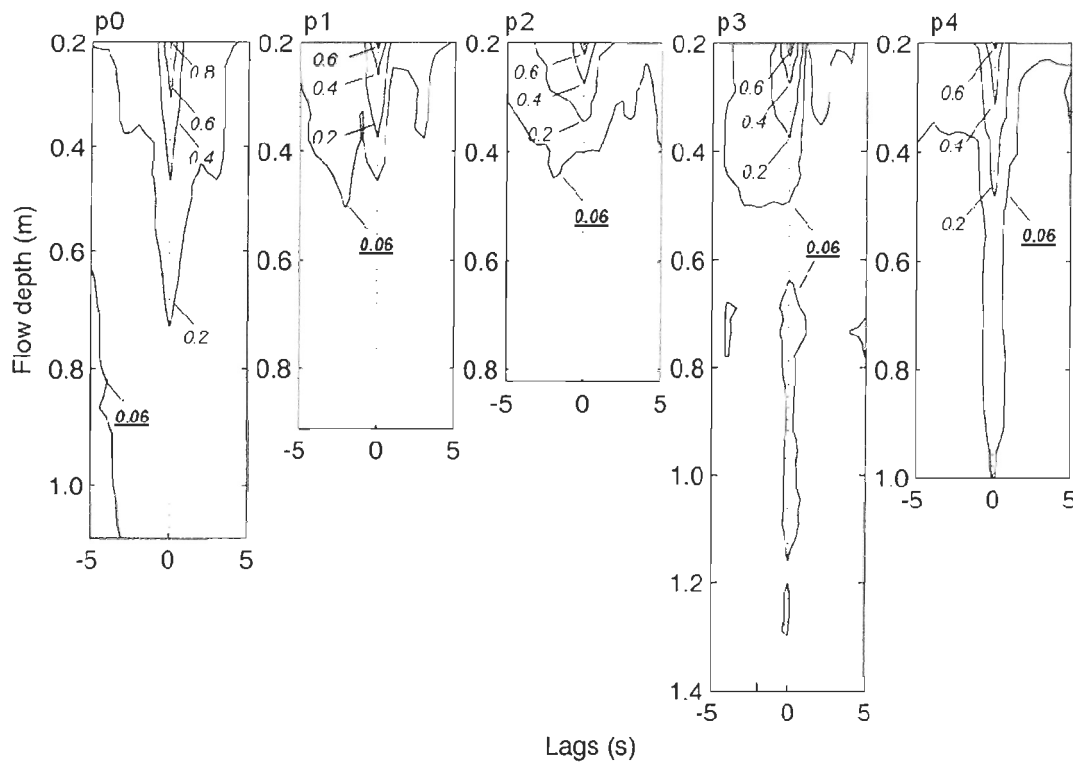


Figure 1.8: Isolines of cross-correlation values between the top third cell from the water surface (or ice cover) and every other downward cells of the profiles. The line labeled 0.06 represents the critical value of statistical significance at  $\alpha = 0.05$ .

### 1.3.5. Correlation matrices

The vertical extent of macroturbulence over the flow depth can be estimated using correlation values from other cells in the profile. Each cell of the profile is successively used as the fixed cell to compute correlation values with all other cells of the profile. The previous cross-correlation analyses based on the third cell from the ice cover showed the absence of definite inclinations in flow structures for both open-channel and ice-covered conditions. This result simplifies the analyses because it is not necessary to consider oblique continuity in correlation values. In other words, we can consider that the maximum correlation values between the time series will occur at a time lag of 0. Values are presented in the form of matrices with axes that represent cell velocities of differing flow depths that are correlated

against each other in the profile. The oblique white line of cells represents perfect correlation between one cell and itself. The information is best read on the vertical where correlation values can be viewed considering successively different cells of the flow. Looking up (water surface) or down (channel bed) from each white cell, correlation values can show the extent of flow that remains correlated. From this, a measure of the vertical extent of coherency ( $d_{corr}$ ) can be calculated, representing the maximal distance before correlation values dip below the threshold for statistical significance. The mean vertical extent of coherency for an entire profile ( $\bar{d}_{corr}$ ) represents the average (in percentage of flow depth) observed for all cells of the profile. These values are presented in table 1.4.

In open channel conditions, correlation values of both the  $u$  and  $v$  components remain statistically significant throughout the entire flow depth for almost all cells ( $d_{corr} = Y$ ). On average, correlation values are of the order of 0.44% and 0.59% for the  $u$  and  $v$  component respectively (considering only significant values and excluding values of perfect correlations). Correlation values vary mainly as a function of the separation distance between the cells and are fairly unaffected by flow depth, although slightly weaker correlation values can be identified toward the water surface compared to the river bed for the  $u$  component. In ice-covered conditions, average correlation values are much lower in comparison to open channel conditions for both the  $u$  and  $v$  components of the flow. Again, values for the  $v$  component are systematically higher than for the  $u$  component. In ice-covered conditions, correlated cells do not cover the entire flow depth ( $d_{corr} < Y$ ). The mean extent of correlated cells ( $\bar{d}_{corr}$ ) for each profile covers 0.58, 0.64, 0.64 and 1 time the flow depth for p1, p2, p3 and p4 profiles, respectively. For the  $v$  component, these values increase to 0.81, 1, 0.91 and 1 time the flow depth.

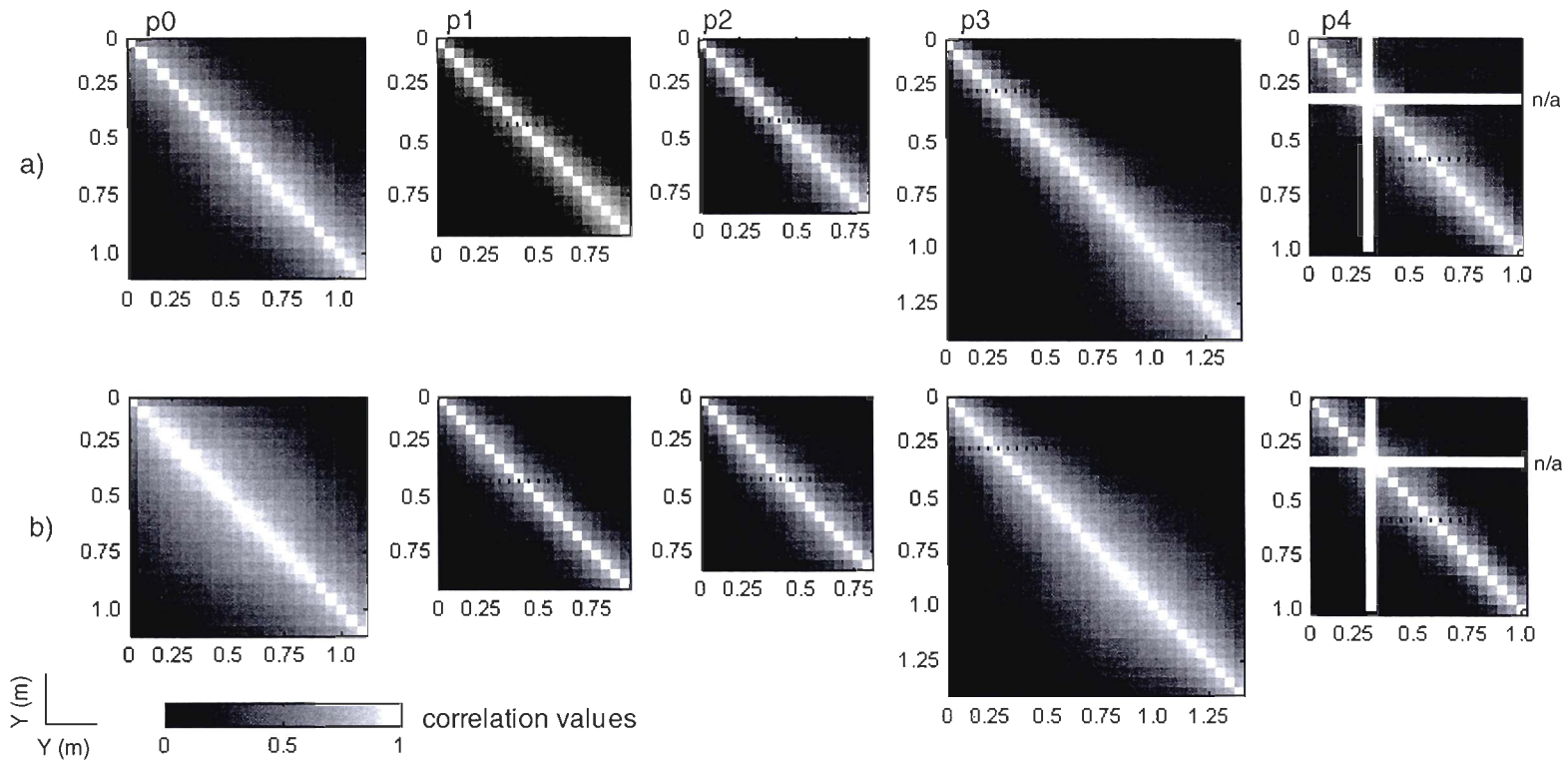


Figure 1.9: Correlation values between the time series of the profile for the a)  $u$  and b)  $v$  component of the flow. Shades of gray represent the intensity of the correlation values between 0 (black: no correlation) and 1 (white: perfect correlation). Values under the critical value for statistical significance at  $\alpha = 0.05$  level were set to 0. The dot line is  $y_{uv=0}/Y$ .

Table 1.4: Mean correlation coefficients and vertical extension of correlated cells in the flow

	p0	p1	p2	p3	p4
$\bar{r}$					
<u>u</u> - velocities	0.44	0.21	0.24	0.28	0.32
<u>v</u> - velocities	0.59	0.28	0.34	0.36	0.38
$\bar{d}_{corr}$					
<u>u</u> - velocities	1	0.58	0.64	0.64	1
<u>v</u> - velocities	1	0.81	1	0.91	1

$\bar{r}$ : Mean correlation coefficients applied to all significant values in the matrices No significant negative correlations were observed.

$\bar{d}_{corr}$ : Mean vertical extent of significant correlation values in the matrices (in proportion of flow depth)

The separation distance between the cell pairs in ice-covered profiles affects the correlation values, but the position of the cells in the water column must also be considered. For an equal separation distance, correlation values vary if the cells are closer to the ice or to the bed. This can be easily seen in the matrices of the *u* component. Profiles p1, p2 and p3 show clear increase in the maximal distance of correlated cells with increasing depth (closer to the bed boundary). Profiles p1 and p2 show a gradual increase while profile p3 shows a clear transition between the two boundaries. There is not a good correspondence between the position of zero Reynolds shear stress and the apparent transitions in correlation values. The only clear correspondence is for the *v* component in profile p3 that presents a sharp transition between the two boundaries. The other profiles exhibit either a gradual change (p1 and p2) or no uncorrelated cell pairs (p4) to establish a match with the plane of zero Reynolds shear stresses. However, the relative thickness of the two boundary layers as derived from both analyses is fairly similar. The larger coherency near the bed as revealed by correlation matrices for profile p1, p2 and p3 is reflected by a shifted position of the Reynolds shear stresses closer to the ice cover.

#### *1.4. Discussion*

The analyses show an overall consistency in the picture of macroturbulence for both open channel and ice-covered channels. In open channel conditions, we are confident that the results show the presence of macroturbulent coherent flow structures as reported in earlier studies that focused at this scale of analysis (Roy *et al.*, 2004). The LISA analyses detected vertically organised stripes of high and low speed coherent motions covering the entire flow depth. The mean length scales of coherency measured from the ACF are estimated at 2.6 times the flow depth, which lies in the range of 2-3 times the flow depth as reported by Roy *et al.* (2004). The two analyses are not necessarily referring to the same scale of macroturbulence, but they both contribute to a complementary view of macroturbulence. LISA illustrates the space-time pattern of coherency while the ACF gives an accurate measure of their size. Discrepancies with past model of large scale coherent structures also appear. Cross-correlations reveal no perceptible tilting in the structure while previous flume and field studies have both shown that macroturbulence should be forwardly inclined in the flow (Brown and Thomas, 1977; Levasseur, 1999; Buffin-Bélanger *et al.*, 2000). However, this assessment should be based on a higher sampling frequency to be adequately resolved. Also, vertical velocities are not displaying the same picture as for the longitudinal velocities. Firstly, clusters of coherent motions are not evenly distributed over flow depth. They are more frequent toward the center of the flow and show a decrease both toward the water surface and the bed. Secondly,  $ITS_v$  and  $ILS_v$  show a gradual decrease toward the water surface. This trend is more in line with the occurrence of smaller scaled coherent structures that form near the channel bed and advects in the outer layer where it coalescences and dissipates.

In ice-covered conditions, velocity profiles adopt classical parabolic shapes with varying symmetry that reflect the influence of the ice cover and of the bed roughness on mean velocities. Negative Reynolds shear stress values indicate the production of turbulence arising from the flow interaction with the ice cover. The position of the inversion between positive and negative Reynolds shear stress value ( $y_{uv=0}$ ) is used to identify a mean interface of turbulent exchanges occurring from each boundary layer. This interface is symmetrical for

profiles p2 and p4 and asymmetrical for profiles p1 and p3, with an accentuate dominance in turbulence production from the bed channel. No obvious roughness feature could explain the variability in asymmetry between the profiles. It is likely that they are related to a spatial pattern at the reach scale (p1 and p3 are located at the centre of the channel while p2 and p4 are closer to one of the channel banks) instead of being related to the roughness features of the ice cover or the channel bed at the very local scale. About macroturbulent coherent structures, the results pinpoint to two complementary views of macroturbulence:

1) On one hand, several results reiterate the flow structure division into two independent TBL: the frequency of clusters detected with LISA for the streamwise velocity component are more defined in the vicinity of the boundaries, ILS are highest close to the boundary walls and matrices of correlation values show vertical discontinuity in flow coherency. These results all converge towards a picture of two boundary layers with high turbulent exchange between the two, thus disrupting macroturbulent coherent structures. Coherency is preferentially located near each of the boundary walls and flow motions associated with coherent structures seem less likely to overlap both boundary layers. The main consequences of this division is that macroturbulence under an ice cover is highly reduced in scale, both streamwise and vertically. The ACF estimates that the streamwise length scale of macroturbulent coherent structures is reduced from an average of 2.6 to  $0.4Y$  ( $u$  component) and from 1.9 to  $0.4Y$  ( $v$  component). Correlation matrices show that the vertical extension is less than the flow depth in ice-covered conditions: between 0.58 to  $1Y$  ( $u$  component) and between 0.81 to  $1Y$  ( $v$  component). Perhaps, each boundary is fed with turbulence production from the flow interaction with the walls and macroturbulence structures advect in the flow with limited capacity to expand into the other territory. It could then be hypothesised that the scale of macroturbulence is determined by the thickness of the respective boundary layers. No particular relation between the scale of macroturbulence and outer layer parameters could be identified. However, it is likely that the macroturbulence structure division in the flow is a function of the roughness ratio between the ice cover and the bed channel at the reach scale. Further studies should use a more explicit notion of roughness ratio between the ice cover and the bed channel to better evaluate its influence in macroturbulence dynamics.

2) On the other hand, it also appears incorrect to present macroturbulence as a confined mechanism limited within each respective boundary layers. The results show that macroturbulence display spatial trends in the form of two boundary regions where coherency is maintained and one fuzzy mixing region where it is disrupted and eventually dissipated. Visualization of velocity coherency using the LISA algorithm revealed clear intermittent overlap of the clusters over both boundaries. The permeability of the interface between the two boundaries is further emphasized from the results of the correlation matrices that presents a mismatch between the position of  $y_{uv=0}/Y$  and the vertical extension of correlated cells in the flow. At first, this could appear as contradictory since one would assume that the position of the mixing layer would imply that velocities would stop being correlated when crossing this interface. However, since it is a mean position, it is possible to imagine a scenario where the macroturbulent structures could be triggered alternatively from the ice cover and the bed channel and still expand throughout both boundary layers. This situation would however necessitate highly quiescent and ephemeral macroturbulent structures. Perhaps, this is the case for profile p4 that presents no uncorrelated cells over the flow depth ( $\bar{d}_{corr} = Y$ ). The results for profile p1, p2 and p3 rather suggest a mid case scenario where macroturbulent structures expand from both boundary layers and maintain their coherency across the mixing layer before breaking up ( $\bar{d}_{corr} < Y$ ). Flume studies have already shown that coherent structures shed in the lee of protruding obstacles attached to the bed can advect as far as the ice cover (Ettema *et al.*, 1999). Hence, vertical exchanges between the two layers may certainly arise for individual small-scaled coherent structures with high momentum. The outer region may then be perceived as a territory where low momentum macroturbulent coherent structures can occupy intermittently. In fact, the idea of a division into two TBL might be misleading when considering macroturbulence dynamics since this so-called frontier is not static in time.

These two complementary views of macroturbulence are conceptually illustrated in figure 10. The division of the flow is represented by two TBL enclosing a mixing region that is shared by the two. In this case, the TBL of the bed is thicker than the TBL of the ice as revealed by the correlation matrices. This can evolve through time as the roughness of the ice undercover changes in the winter season and the roughness ratio with the bed is modified (Ashton and

Kennedy, 1972). Both TBL present velocity signatures of ejection and incursion type motions that are conveyed in the mixing region along with macroturbulence coherent structures. Macroturbulent coherent structures are represented as motions attached to either boundary walls penetrating to various extents into the mixing region. Their length decreases from the boundary walls towards the mixing region, but they can extend far into the flow and even reach the opposite boundary. The representation of macroturbulent coherent structures through time is only tentative, but appears as patchy as revealed from the LISA analysis. Further studies should regard with more emphasis the organisation and structure of macroturbulent coherent structures in the time and frequency domains.

These two complementary views of macroturbulence are conceptually illustrated in figure 1.10. The division of the flow is represented by two TBL enclosing a mixing region that is shared by the two. In this case, the TBL at the bed is thicker than the TBL under the ice cover. This can evolve through time as the roughness of the ice undercover changes in the winter season and the roughness ratio with the bed is modified [*Ashton and Kennedy, 1972*]. Both TBL present velocity signatures of ejection and incursion type motions that are conveyed in the mixing region along with MCS. MCS are represented as motions attached to either boundary walls penetrating to various extents into the mixing region. Their length decreases from the boundary walls towards the mixing region, but they can extend far into the flow and even reach the opposite boundary. The organization of MCS through time is only tentative, but appears as patchy when referring to results from the LISA analysis. Further studies should examine with more emphasis the organisation and structure of MCS in the time and frequency domains.

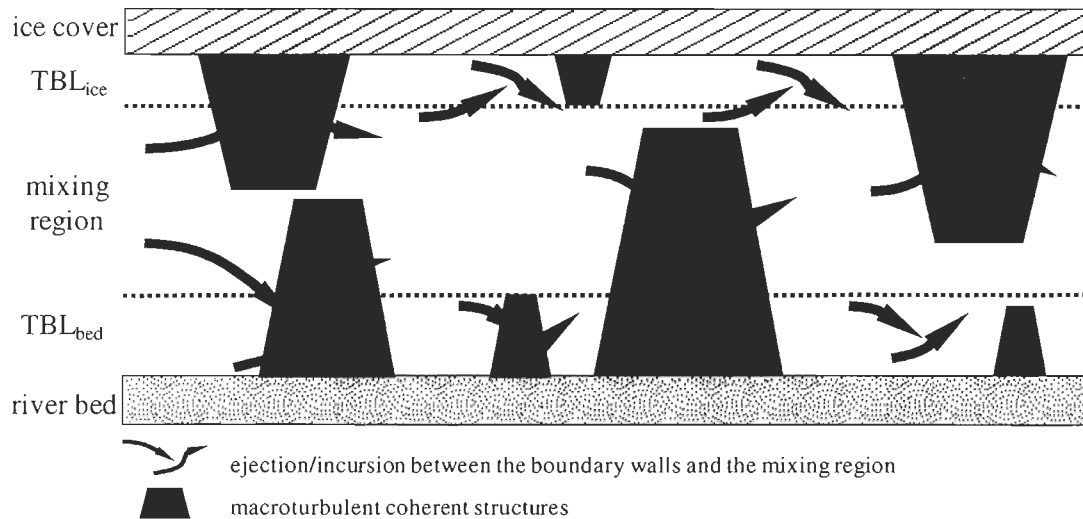


Figure 1.10: Conceptual model of macroturbulent coherent structures under an ice cover

### 1.5 Conclusion

This paper aimed at detecting and observing macroturbulent coherent structures under an ice cover in a sand bedded river. This was possible using a pulse coherent acoustic Doppler profiler which can sample water velocities simultaneously over the entire flow depth at a high vertical resolution. This allowed for detailed observations of macroturbulence in response to the presence of an ice cover. The ice cover exerts a friction that forms an upside down boundary layer. The four ice-covered profiles exhibit velocity profiles with parabolic shape of varying asymmetry. Reynolds shear stresses in the  $uv$  plane show positive values near the channel bed and negative values near the ice cover. This allowed identifying a mean mixing layer dividing two TBL, each one dominated by a turbulence signature referring to either the ice cover (top boundary) or the channel bed (bottom boundary). The LISA algorithm revealed vertical stripes of high and low speed coherent motions in both open channel and ice covered flows. In the presence of an ice cover, clusters are less frequent and best defined in the vicinity of the boundary walls. Presumably, each boundary wall generates and sustains its own set of macroturbulent motions that compete with each other in the outer region of the flow where they become scarcer and less persistent. As a consequence, ice-covered flow is

more complex and macroturbulent coherent structures are reduced in scale. The ACF showed that the streamwise length scale is highly reduced and correlation matrices revealed that their vertical extension is less than the flow depth. However, the flow structure must not be perceived as two compartmental regions with closed frontier. Coherent motions do overlap both boundary layers, however less often and with reduced coherency. Further measurements aimed at the scale of macroturbulence are most needed, especially with instruments with higher space-time resolutions, to further specify the interactions at the interface between the two TBL.

## *CHAPITRE II*

### *HELICAL CELL MOTIONS IN A SMALL ICE-COVERED MEANDER RIVER REACH*

#### *CELLULES HÉLICOÏDALES DANS UN MÉANDRE DE RIVIÈRE EN PRÉSENCE D'UN COUVERT DE GLACE*

##### Abstract

The investigation of the flow field with a Pulse-Coherent Acoustic Doppler Profiler has led to new high resolution observations of the secondary flow pattern occurring in a natural ice-covered meander reach. Surveys were conducted during two successive winter periods with different ice conditions. Massive frazil ice accumulation was present during one of the survey and its influence on the flow pattern could be assessed. Results show that the primary flow is clearly deflected toward the outer bend. Secondary flows are one order of magnitude less than the primary flow and they display two stacked counter rotating helical cells pattern occurring at the entrance of the bend. This pattern is associated with the parabolic shape of the velocity profiles entering the bend. The pattern rapidly evolves downstream, reducing to one helical cell rotating in an opposite direction than what is observed in open channel flows. Flow mixing and morphological non-uniformity are potential factors governing the development of the helical cells throughout the bend. Our observations show that a similar coherent flow pattern rapidly forms downstream of a massive frazil ice obstruction in the bend. Frazil ice does not constrain the formation of helical flow pattern in river bends.

### Résumé

Le patron des écoulements secondaires dans un méandre en présence d'un couvert de glace est révélé par des mesures à haute résolution obtenues à l'aide d'un profileur acoustique à effet Doppler. L'échantillonnage du champ de vitesses s'est déroulé pendant deux hivers successifs qui présentaient des conditions de glace différentes. La présence d'accumulations massives de frasil à l'apex du méandre lors de l'une des campagnes a permis de mesurer son incidence sur le patron spatial des écoulements secondaires. En l'absence de frasil, l'écoulement principal est dévié rapidement vers la berge externe en réponse à l'accélération centrifuge. Les écoulements secondaires sont en moyenne un ordre de grandeur plus faible que l'écoulement principal. À l'entrée du méandre, ceux-ci sont caractérisés par la présence de deux cellules hélicoïdales superposées. Ce patron est associé à la forme parabolique des profils de vitesses présents sous couvert de glace. Ce patron est rapidement réduit à la présence d'une seule cellule secondaire avec un sens de rotation opposé à celui attendu dans les méandres à surface libre. Cette évolution du patron peut être associée au mélange des écoulements et à la non-uniformité morphologique d'un méandre caractéristique des milieux naturels. Dans la période caractérisée par une accumulation de frasil, l'écoulement secondaire est formé de deux cellules hélicoïdales superposées dès la sortie de la zone de confinement. L'accumulation de frasil n'apparaît donc pas comme une contrainte persistante pour leur formation.

## *2.1. Introduction*

Flow structure in open channel meander bends has long attracted attention (Thomson, 1876) and is still extensively studied in both laboratory flume (Blanckaert and Graf, 2001) and field experiments (Frothingham and Rhoads, 2003). Planform curvature of meandering bends promotes strong secondary currents that develop into helical patterns. This pattern is coincident with high shear stress directed towards the outer bend (Bathurst et al., 1979) and is connected with the erosion and deposition pattern occurring at the meander reach scale (Bridge and Jarvis, 1982). Flow helicity is governed by two opposing forces that balance differently along flow depth. Bend curvature is linked to a centrifugal acceleration that works to direct the water toward the outer bend. Skewing of the flow toward the outer bend raises the water surface thus creating a cross-sectional difference in water surface height. The pressure differential induced from the water surface height gradient works to redirect the water toward the inner bend. Given that average flow velocities tend to follow a logarithmic vertical profile in a shallow flow, high speed velocities at the water surface are more affected by the centrifugal acceleration and directed toward the outer bend. The low speed flow near the channel bed is less affected by centrifugal acceleration compared to the pressure force and hence is directed toward the inner bend. This twofold mechanism induces a rotating motion progressing downstream that can be grossly represented as a helical pattern. In spite of the crucial role of the vertical distribution of flow velocities, the helical flow pattern was shown to be resilient to the shape of the velocity profile in the flow entering the bend in open channels (Ghamry and Steffler, 2002).

Ice-covered flow is drastically different from open channel conditions. Depth-limited ice-covered channels are characterized by two distinct boundary layers developed in the opposite direction and stacked on top of each other. Each velocity gradient is affected by the roughness of its boundary and meets at some point in the water column where maximal average velocities are found. The vertical distribution of average flow velocities has a parabolic shape. Urroz (1988) and Zufelt (1988) have both studied the flow field in flumes reproducing highly curved river bends with an ice cover. By investigating the lateral components of the velocity profiles, the authors have found evidence of two stacked counter

rotating helical cell motions. High speed flow occurring at mid-depths of the water column is preferentially deflected toward the outer bend by centrifugal acceleration. Flow redirection toward the inner bend occurs near both the ice and channel boundaries. This results in two counter rotating helical cell patterns.

The occurrence of two helical cells in natural ice covered meander reaches has yet to be observed in small rivers. Natural conditions are expected to offer more complexity because of the irregularity in bed morphology and in ice cover thickness and of the potential obstruction in the meander from frazil particle accumulation. Velocity measurements are needed to feed models describing ice-covered river flow structure, but also to assess the ubiquity of the helical flow model in different natural settings and ice conditions. However, the lack of adequate instruments has long impeded this type of survey. The Pulse-Coherent Acoustic Doppler Profiler (PC-ADP) is a relatively new option for field surveys that can measure entire velocity profiles simultaneously in the three components of the flow. This instrument offers the opportunity to sound a vast volume of flow with good spatial and temporal resolution. In this study, surveys have been conducted in two successive winter periods in a small meandering reach. The surveys allowed us to 1) detect and characterize the presence of helical cell motions and 2) to assess the variability of the flow structure during two successive winter conditions. The occurrence of massive frazil ice accumulations in the river bend during the first survey gave us an insight on the sensitivity of the average flow structure to this frequent winter related process.

## *2.2. Methodology*

Field surveys were carried out in early March 2007 and 2008 in a small meandering reach of the Neigette River, a tributary of the Mitis River (Quebec, Canada). The meander reach is deeply incised and stabilized by compact clay deposits. Bed material is composed of sand. Discontinuous ripples were locally observed on the bed at the head of the pool. The radius of curvature is low (~50 m) and results in a sharp 134° change in talweg orientation (figure 2.1a).



more likely to develop. Figure 2.1a summaries the sampling design in which profiles are identified by their relative position along a particular CS measured from the outer bend.

Velocity profiles were collected using a Sontek 1.5Mhz Pulse Coherent Acoustic Doppler Profiler (PC-ADP). The profiler has the ability to collect simultaneously entire velocity profiles in all three velocity components (longitudinal, lateral and vertical). The PC-ADP relies on a particular measurement technique, the coherent mode, that can provide a vertical resolution in the order of a few centimetres (Lacy and Sherwood, 2004). The instrument sends two short sound impulses in the water column where it is backscattered by the buoyant particles in movement within the water. Velocities are measured parallel to three radial beams inclined at  $15^\circ$  with respect to the axis of the instrument, forming a sampling volume extending outward in the water column following the shape of a cone (figure 2.1b). The instrument measures velocities at several depths of flow which corresponds to slices (cells) of the cone. The sampling diameter of the cells grows with distance from the instrument ( $d$ ) as a ratio of  $\sim 0.5d$ . Velocities are converted into a cartesian framework which postulates that the flow measured by all beams is spatially equivalent, *i.e.* flow is assumed to be homogeneous within the sampling volume.

We used a tripod mount with a scaled rod which allowed us to insert the instrument head even with the ice undercover. Blanking distance, the no-see area near the nose of the instrument, was set to its minimum length of 0.05 m and cell heights varied between 0.044 or 0.105 m. Velocities are sampled at a frequency of 1 Hz during 10 minutes. Along with velocity data, the instrument measures quality parameters for validation purposes. Correlation values measure the coherency between each sound impulses pair (Sontek, 2004). No minimal threshold is recommended since correlation value is also function of environmental conditions. Interference between successive sound impulses typically hinders the capacity of the PC-ADP to resolve the cells nearest to the bed. We have found that the ice cover further increase sound interferences and diminish correlation to values as low as 25%. We systematically removed time series that presented lower mean correlation values ( $<15\%$ ) and these appeared to be systematically close to the bed where flow is also less homogeneous. Time series are also affected by ambiguity error that results from the short range of

resolvable velocities (Lhermitte and Serafin, 1984). This is overcome by the use of an independent velocity measurement to detect and correct the corrupted data. The algorithm provided by Lacy and Sherwood (2004) and improved by Cassista (2007) was applied to all time series and proved to be effective for correcting ambiguity errors. Time series were averaged and rotated to allow the analysis of the lateral components, which are defined as the perpendicular to the primary flow velocities. The rotation used herein is applied to every profile of each CS to give a net zero lateral discharge (Markham and Thorne, 1992a,b). The technique is known to yield a better representation of the true secondary components of the flow as opposed to the more commonly used Rozovskii (1954) rotation technique (Lane et al., 2000).

## **2.3. Results**

### *2.3.1. Ice cover and velocity profiles*

Figure 2.2 illustrates the spatial variability of ice cover thickness and roughness classes for both surveys. Ice thickness at the reach scale ranges from 51 to 76 cm and from 53 to 69 cm for the 2007 and 2008 surveys respectively. Despite the similarity in range, the first survey presents a more scattered spatial organisation. Ice thickness is patchier and presents more drastic local changes in 2007. This patchiness at the reach scale is matched by the visual ice undercover roughness at the local scale. The rough category represents 48 % of observed sites in 2007 as opposed to 16% for the 2008 survey. Also, at the time of measurement in 2007, the pool area was filled with accumulated frazil ice particles that often hindered the assessment of the undercover state as well as the measurement of velocity profiles. The accumulation of frazil particles acts as a porous roughness that is known to modify the pattern of flow in a meander bend (Sui et al., 2008). Thus, it is expected that flow structures between the two successive winters might exhibit different patterns.

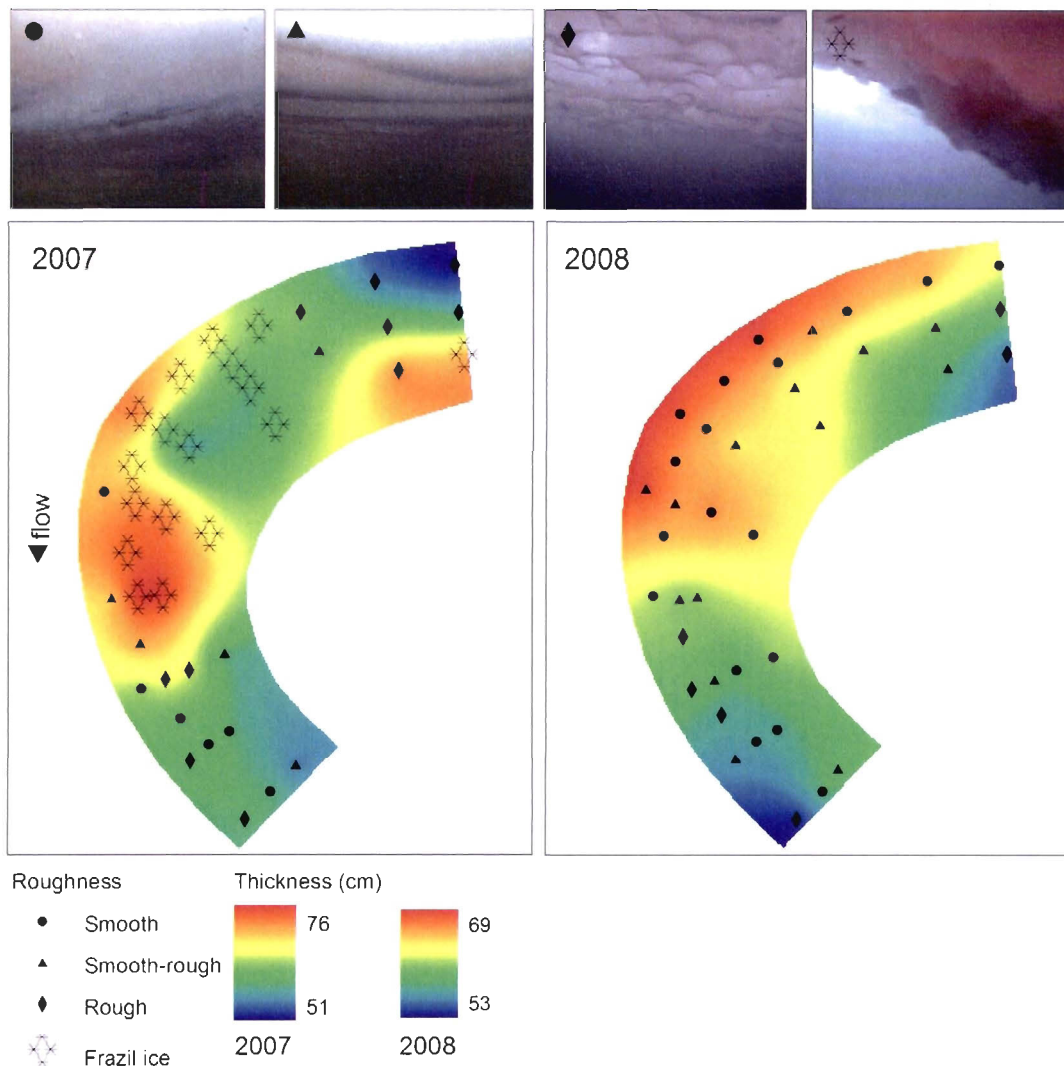


Figure 2.2 : Ice cover thickness and undercover roughness for the 2007 and 2008 surveys.

Figure 2.3 presents two velocity profiles collected during each survey at the entrance of the pool where flow is still lightly affected by centrifugal acceleration. The two surveys show differences in flow depths and velocities due to the different discharge, but the profiles entering the bend present a classical parabolic shape typical of river flow under an ice cover. Also, the ice undercover is rougher at the entrance of the bend in 2007. As a result, profile at position  $8^{\circ}-1/2$  (2007) has a shape with maximum velocities found closer to the bed. Undercover roughness may shift the position of maximum velocities and so influence the

height of flow divergence against the outer bend. Overall, the profiles entering the bend exhibit classical undercover profiles that would theoretically lead to two helical cell motions (Urroz and Ettema, 1994).

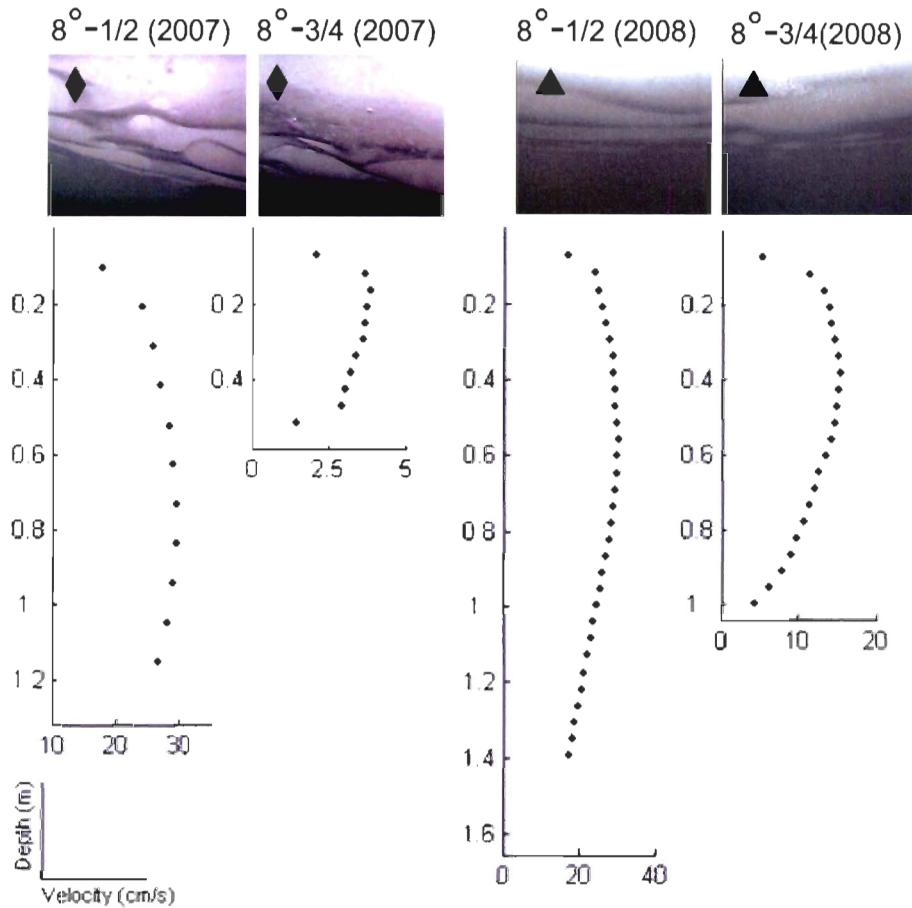


Figure 2.3 : Velocity profiles at the entrance of pool for the 2007 and 2008 surveys.

### 2.3.2. Three dimensional flow pattern

The planform view of depth-averaged flow velocities throughout the bend is illustrated in figure 2.4 for the 2008 survey. Although the figure does not show the complex vertical flow pattern that could be typical of flow in meander bends, several features can be observed. At the bend entrance ( $0^\circ$  and  $8^\circ$  CS), average flow velocities are in the order of  $\sim 25$  cm/s with a

clear mean deflection toward the outer bend. The deflection is observed for downstream CS and a line of maximum velocity develops in the reach towards the outer bend. A peculiar velocity signature occurs near the 8° CS close to the outer bend where near null velocities are observed with a recirculation pattern (not visible on the figure because of the scaling). The low velocity values are caused by the presence of a tree along the outer bank that was revealed by the underwater camera during the survey. The wake effect of this obstruction can be perceived from slower velocities measured near the outer bank at 17° CS and 23° CS. As the flow enters the bend, flow velocities are gradually slowed to ~10 cm/s near the deepest part of the pool and then rapidly speed up again from the 105° to 134° CS where flow depth is rapidly reduced. Flow is highly non-uniform throughout the bend.

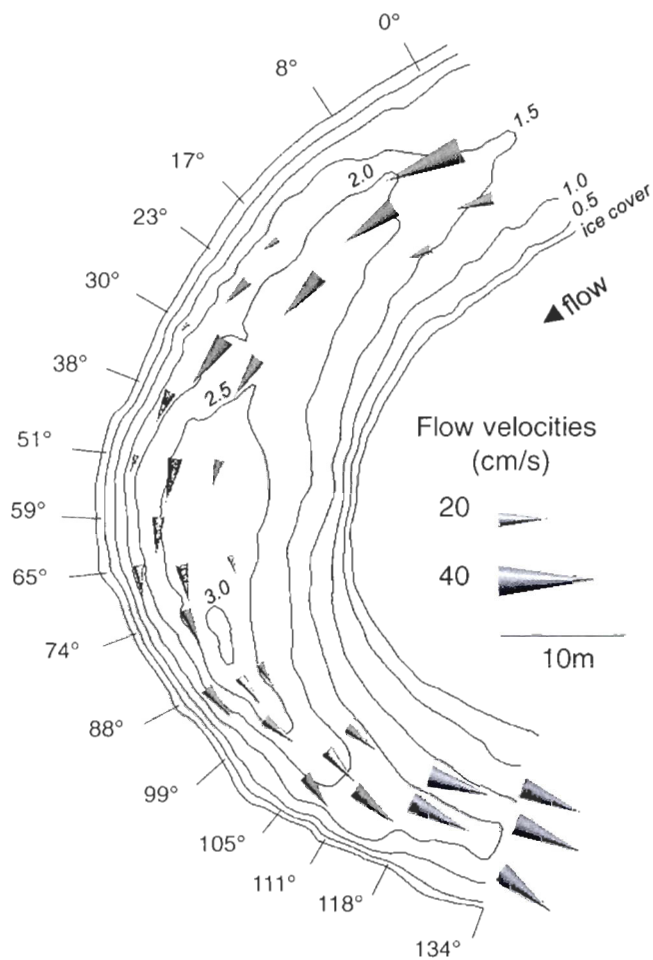


Figure 2.4 : Planform view of depth-averaged flow velocities of the 2008 survey.

Figure 2.5 illustrates flow velocities along five cross-sections ( $30^\circ$  to  $105^\circ$ ) near the apex of the meander for the 2008 survey, downstream from the perturbation caused by the tree obstruction. From bottom to top, the cross-sections show the downstream evolution of three dimensional flow patterns where colors and vectors represent respectively the downstream (u) and joint lateral (v) and vertical (w) average velocity components of flow. From the combination of vectors and colors, a secondary flow pattern is observed along a velocity profile when clear lateral and vertical velocity changes occur in a coherent fashion. For an easier lecture, a schematic view of the orientation of the vectors is shown on the right hand side of the figure. Although it closely follows the pattern exhibited by the measured vectors, this schematic view is an interpretation by the authors of the likely pattern observed and is not scaled with the magnitude of secondary flow. Looking at the primary component of the flow, downstream maximal average velocities are located near the outer bank throughout the bend as observed in figure 2.4. A shift can be seen while progressing downstream as the location of maximal velocities is moving more closely toward the outer bank edge. Following the expected shape of velocity profiles under the ice cover, maximal velocities are found to be almost consistently at mid-depths of the flow. However,  $88^\circ$  CS and  $105^\circ$  CS differ from this general pattern as maximal velocities are found to lie closer to the ice cover near the outer bank edge.

The secondary component of flow is one order of magnitude smaller than the primary component, in a proportion ranging between 5.3% and 11.2%. The relative magnitude of secondary flow is strongest at the meander apex (11.2%;  $65^\circ$  CS) where primary flow is the slowest due to increased depth and where helical cells are better developed because of the sharp curvature of the channel. Evidence of helical like motions first appears at the  $30^\circ$  CS where profiles in the 1/3 and 1/2 positions show a clear mid-depth deflection toward the outer bend as well as two inward motions near both the ice and bed boundaries. Downstream from this cross-section, the secondary flow pattern is less coherent. Profile at the position 1/3 on the  $51^\circ$  CS also appears to follow a helical cell pattern, although the lateral extent of the cell remains unknown. Profiles along the  $65^\circ$  CS and  $88^\circ$  CS still show a mid-profile deflection in the outward direction while near ice flow remains directed toward the inner bend. However,

near-bed secondary flows are not apparent. Profile at the position  $1/3$  of the  $65^\circ$  CS suggests a potential inward flow near the bed, although this interpretation is tentative due to the lack of information located very close to the bed. Profiles along the  $88^\circ$  and  $105^\circ$  CS present mid-depth and near-bed flow directed toward the outer bend while near-ice flow is directed toward the inner bend. This pattern suggests the presence of only one helical cell rotating in a counter clockwise direction. Secondary flows past the  $105^\circ$  CS show no apparent coherent pattern.

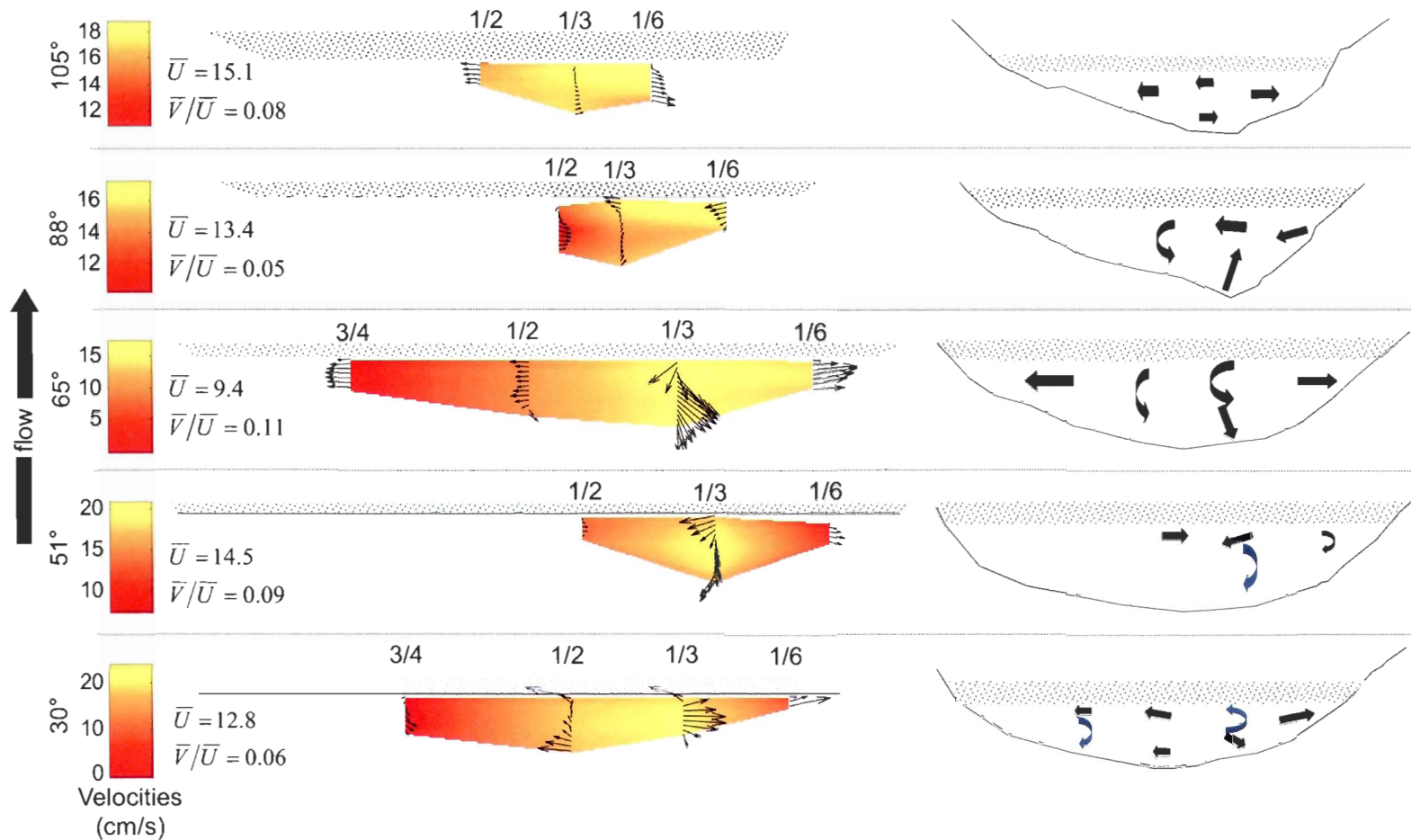


Figure 2.5 : Longitudinal (colored contours) and secondary flow patterns (vectors) viewed downstream from bottom to top (2008 survey). One vector is presented for each three measurements (0.13 m apart from each other on the vertical axis). Right handed schemes are a synthesis of results for a better reading.

During the 2007 survey, frazil ice particles obstructed a large volume of the bend, thus no velocities have been measured in the pool area. However, the PC-ADP allowed us to assess indirectly the thickness of frazil ice accumulation by analyzing the strength of the backscattered signal. Strong rebound clearly identified area of frazil ice accumulation. Figure 2.6 is a representation of frazil ice obstruction and flow velocities along the 65°, 88° and 105° CS of the 2007 survey. Frazil ice is shown to be mainly confined toward the inner bend or near the talweg. Velocities measured at the exit of bend (105° CS) show a surprisingly coherent motion despite the upstream obstruction caused by the presence of frazil ice. Profile at position 1/3 shows two near-bed and ice inward motions suggesting the presence of two helical cells. Profile at position 1/2, at the innermost edge of the bend, shows a closed rotation cell which suggests that the pattern consisting of two helical cells is limited to the outer half of the bend.

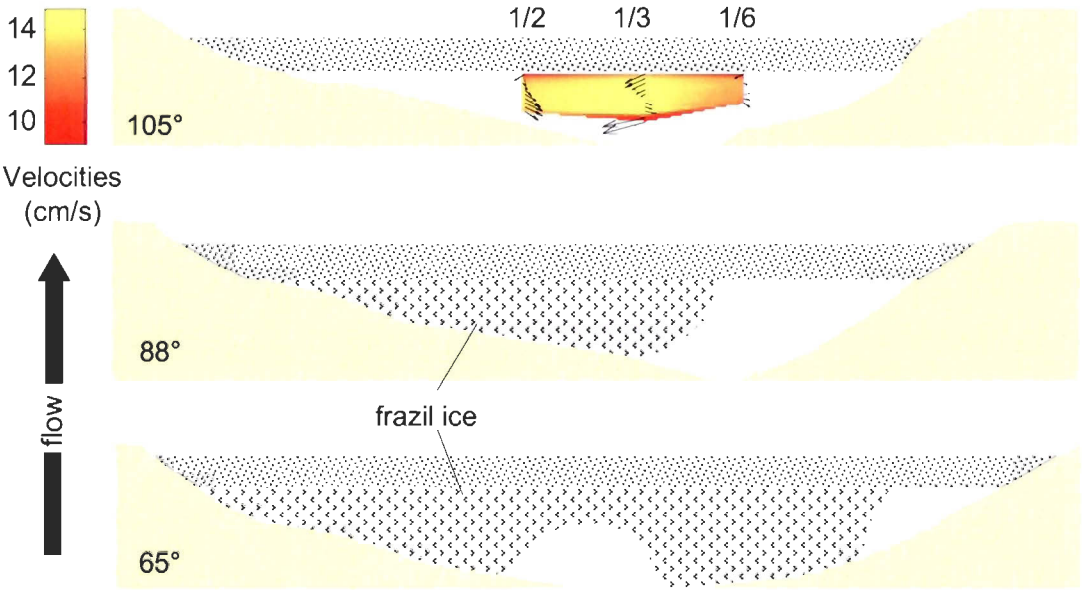


Figure 2.6 : Frazil ice obstruction and flow velocities in the pool area of the 2007 survey

#### *2.4. Discussion*

These results suggest that two stacked helical cell motions are present in the river bend under an ice cover. However, data from the 2008 survey reveal a discontinuous pattern as the flow is advecting downstream. The two helical cells are clearly observed between the 30° and the 51° CS, but the pattern is rapidly modified further downstream. At the meander apex (65° CS), strong secondary flow suggests only one helical cell rotating in a counter clockwise direction, which is on the opposite direction of what is expected under open channel flow conditions. The single helical cell pattern is less coherent but still apparent at further cross sections downstream. This complex evolving pattern is unexpected considering the results of past studies assessing the helicity of flow in ice-covered flumes, where two stacked counter rotating helical cell motions were observed throughout the entire bend (Urroz, 1988; Zufelt, 1988). Concerning the counter clockwise helical cell, Corney et al. (2006) have also documented in submarine channel meanders a helical motion rotating in an opposite direction from the one found in typical subaerial open channels. They explained the pattern by the presence of density currents exhibiting velocity profiles with maximum speed located near the channel bed (Felix, 2002). The effect of centrifugal acceleration is thus more pronounced near the bed, which is followed by helical rotation in a reverse direction. Although the patterns documented by Corney et al. (2006) are similar to the one we have observed under an ice cover, they are likely resulting from different processes. The vertical velocity profiles entering the bend of an ice covered channel present a parabolic shape with the maximal velocities found near the middle part of the flow (Figure 2.3). Also, because the two helical cell motions take place at the entrance of the bend, the possibility of any persisting helical rotation coming from upstream bends can be discarded.

Urroz and Ettema (1994) have stated that the two helical cells should not be seen as independent, but rather as interacting objects that are likely to become more complex as they develop downstream. The interaction between the cells limits the capacity to describe the phenomenon accurately with the simple hypothesis of two boundary layers sandwiching maximal velocities at mid-depths of flow. Greater complexity in the interaction between the cells may lead to a weaker overall coherency that may feature several competing vorticity

elements. Local higher momentum might favour one or the other cell that will grow at the expense of the other and modify the initial pattern of flow. As the flow is redistributed throughout the bend by secondary currents, the momentum of maximum velocities is also expected to move through the bend. The effect of centrifugal acceleration is evolving coincidentally with the change in the primary flow velocity distribution. Thus, the secondary flow pattern can only be expected to change while moving downstream. The downstream progression can also be affected by the non-uniformity of the channel bed morphology. The discrepancy of our results when compared to flume studies arises most likely from the more complex bed morphology of natural settings. Maximum velocities at 105° CS are nested in the corner formed by the water surface and the outer edge of the bend. This situation most likely result from the sudden change in channel curvature observed at the outlet of the bend (from 65° to 105° CS) that also coincides with a more asymmetrical shape of the cross-sections. The position of maximum velocities and helical pattern found at this cross-section is counter-intuitive since high-speed flow at the water surface would imply flow deflection toward the outer bend instead of inward. Hence, the link between the velocity profile shapes and secondary flow patterns is not simple. The upstream flow redistribution, change in bend curvature and morphological forcing are all acting together throughout the bend to affect the development of a secondary flow pattern as it progresses downstream.

The observations from the 2007 survey have shown the presence of two counter rotating helical cells at the exit of the pool, albeit being significantly obstructed by an accumulation of frazil ice particles. This suggests that frazil ice is not impeding the development of helical type motions. Throughout the bend, the flow pattern is most likely affected by centrifugal acceleration while being simultaneously spatially directed to frazil free areas. Moreover, constriction most likely speeds up flow velocities, enhancing centrifugal effect and helical cell formation. Sui et al. (2008) made measurements inside a bend with a hanging dam of frazil ice that have revealed helical cells to effectively occur amid the frazil free areas of the bend, although the global pattern that was observed was very complex. A flow pattern recovering from this containment might also be further disrupted because of the likelihood of a recirculation area near the inner bend created by the frazil obstruction. With more closely spaced cross-sections, it might be possible to better capture the transition between these areas

and specify the effects of containment on the pattern of flow. The presence of two stacked helical cells at 105° CS during the 2007 survey can be puzzling when only one was observed during the 2008 survey at this location. This implies that the upstream flow pattern has an incidence on the development of the helical cell motions immediately downstream.

### ***2.5. Conclusion***

Investigation with a PC-ADP of the velocity field in a small meandering river reach covered with ice has led to new observations on the pattern of secondary flows in curved channels. Results show evidence of two stacked counter-rotating helical cell motions occurring at the entrance of the bend (30° CS to 51° CS). This pattern evolves rapidly downstream, transforming to one helical cell rotating in an opposite direction than the one expected in open channel flows (61° CS to 105° CS). Flow mixing and morphological non-uniformity are suggested as possible factors explaining the development of the two helical cells into one as it progresses downstream. Frazil ice accumulation in the bend is not an obstacle to the development of the helical cells immediately downstream.

The results emphasise the complexity of flow structures found in ice covered curved channels and its variability in the presence of frazil ice obstructions. The model proposed from flume studies presenting the three-dimensional flow pattern as a set of two closed helical cell motions is likely to oversimplify the complexity of flow occurring in rivers. Further studies should consider increasing the density of velocity measurements in order to better delineate the features of the helical pattern. Also, diversifying the characteristics of the study sites should be considered to analyse flow pattern consistency over different flow and ice conditions. A larger spatial coverage including multiple successive bends could also provide a broader understanding of the flow structure of meandering rivers under ice.

## *CONCLUSION*

Cette étude vise à décrire les impacts du couvert de glace sur la structure turbulente des écoulements en rivière. Nous nous sommes attardés à deux échelles spécifiques, soit les structures macroturbulentes et le patron spatial des écoulements secondaires dans un méandre. En apparence, ces objectifs sont dissociés par le large écart d'échelle qui les sépare. Toutefois, tous deux relèvent directement de l'effet de la glace sur la structure de la CLT de l'écoulement, dont les impacts se transposent à une large gamme d'échelles de temps et d'espace.

Le premier article présente des observations sur l'impact du couvert de glace sur les structures macroturbulentes. Les résultats indiquent que la présence des structures macroturbulentes est calquée sur la division de l'écoulement en deux CLT. Les structures macroturbulentes sont présentes à proximité des plans de rugosité, et inversement, se raréfient à l'interface entre les deux couches-limites. En conséquence, l'échelle des structures macroturbulentes est réduite, possiblement en fonction du rapport de rugosité entre la glace et le lit du chenal à l'échelle du tronçon fluvial. Toutefois, cette division n'est pas une frontière imperméable et des échanges turbulents se produisent entre les deux régions, contribuant au mélange et à la destruction des structures cohérentes de chacune des régions.

Le deuxième article présente en détail le patron tridimensionnel du champ de vitesses à l'échelle d'un méandre. À l'entrée de la courbure, les écoulements secondaires amorcent deux mouvements hélicoïdaux superposés et de rotation opposée. Ce patron résulte de la distribution parabolique des vitesses moyennes sur la profondeur, *i.e.* de la double couche-limite de l'écoulement. À l'apex du méandre, les cellules hélicoïdales se développent en une seule cellule de rotation inverse par rapport au patron observé dans les écoulements de surface. Cette cellule se dissipe rapidement à la sortie du méandre. Le patron global des

écoulements secondaires se distingue des résultats obtenus en laboratoire. La relation entre la structure de la CLT et le développement des cellules hélicoïdales est complexe, conjointement contrôlée par la forme du chenal et l'interaction entre les deux cellules hélicoïdales. La présence de frasil dans le méandre contraint localement les écoulements, mais n'empêche pas le développement des cellules hélicoïdales à la sortie du méandre.

Cette étude permet de rendre compte de l'ampleur des changements conséquents à la présence d'un couvert de glace sur la structure turbulente des écoulements en rivière. L'approche terrain privilégiée ici fournit des indices concrets quant à la complexité des échanges aux deux échelles d'analyse. Dans l'état actuel des connaissances, ces observations ont une teneur exploratoire. Elles révèlent à tout le moins que les connaissances acquises par les travaux en condition libre de glace ne peuvent être transposées directement aux environnements fluviaux englacés. Le cas des rivières englacées exige une bonification des connaissances basée sur une multiplication des observations effectuées dans différentes conditions d'écoulement sous glace, mais surtout une meilleure compréhension des mécanismes.

## RÉFÉRENCES

- Allard, G., T. Buffin-Bélanger et N. Bergeron. 2009. «A conceptual model on the interactions between fluvial and river ice dynamics». Affiche présentée au 15<sup>ème</sup> atelier du CRIPE, 14 au 17 juin, St. John's, Terre-Neuve et Labrador, Canada.
- Anselin, L. 1995. «Local indicators of spatial association – LISA». *Geographical Analysis*, vol. 27, no 2, p. 93-115.
- Ashton, G. D. 1986. *River and lake ice engineering*. Littleton: Water Resources Publications, 485 p.
- Ashton, G. D. et J. F. Kennedy. 1972. «Ripples on underside of river ice covers». *Journal of the hydraulic division*, ASCE, vol. 98, p. 1603-1624.
- Bathurst, J. C., C. R. Thorne et R. D. Hey. 1979. «Secondary flow and shear stress at river bends». *Journal of hydraulic division*, ASCE, vol. 105, p. 1277-1295.
- Best, J. L. 1993. «On the interactions between flow structure, sediment transport and bedform development: some considerations from recent experimental research». In *Turbulence: perspectives on flow and sediment transport*, sous la dir. de N. J. Clifford, J. R. French et J. Hardisty, p. 61-92. Chichester: Wiley.
- Blanckaert, K. et W. H. Graf. 2001. «Mean flow and turbulence in open channel bend». *Journal of hydraulic engineering*, vol. 127, no 10, p. 835-847.
- Bridge, J. S. et J. Jarvis. 1982. «The dynamics of a river bend: a study in flow and sedimentary processes». *Sedimentology*, vol. 29, p. 499-541.
- Buffin-Bélanger, T., A. G. Roy et A. D. Kirkbride. 2000. «On large-scale flow structures in a gravel-bed river». *Geomorphology*, vol. 32, p. 417-435.
- Buffin-Bélanger, T., A. G. Roy et M. Lévassieur. 2001. «Interaction entre les structures d'échappement et les structures à grande échelle dans l'écoulement turbulent des rivières à lit de graviers». *Revue des sciences de l'eau*, vol. 14, p. 381-407.
- Carling, P. A. 1992. «The nature of the fluid boundary layer and the selection of parameters for benthic ecology». *Freshwater Biology*, vol. 28, p. 273-284.

- Cassista, A. 2007. «L'utilisation du PC-ADP (Pulse-Coherent Acoustic Doppler Profiler) dans un écoulement turbulent en rivière peu profonde». Mémoire de maîtrise, Montréal, Université de Montréal, 156 p.
- Cellino, M. et U. Lemmin. 2004. «Influence of coherent flow structures on the dynamics of suspended sediment transport in open-channel flow». *Journal of hydraulic engineering*, vol. 130, no 11, p. 1077-1088.
- Corino, E. R. et R. S. Brodkey. 1969. «A visual investigation of the wall region in turbulent flow». *Journal of Fluid Mechanics*, vol. 37, p. 1-30.
- Corney, R. I. T., J. Peakall, D. R. Parsons, L. Elliott, K. J. Amos, J. L. Best, G. M. Keevil et D. B. Ingham. 2006. «The orientation of helical flow in curved channels». *Sedimentology*, vol. 53, p. 249-257.
- Davis, J. A. et L. A. Barmuta. 1989. «An ecologically useful classification of mean and near-bed flows in streams and rivers». *Freshwater Biology*, vol. 21, p. 271-282.
- Defina, A. 1996. «Transverse spacing of low-speed streaks in a channel flow over a rough bed». In *Coherent Flow Structures in Open Channels*, sous la dir. de P. J. Ashworth, S. J. Bennett, J. L. Best et S. J. McLelland, p. 87-99. Chichester: John Wiley.
- Drake, T. G., R. L. Shreve, W. E. Dietrich, P. J. Whiting et L. Leopold. 1988. «Bed-load transport of fine gravel observed by motion picture». *Journal of fluid mechanics*, vol. 192, p. 2193-2217.
- Ettema, R., M. Muste et S. Coleman. 1999. «Flume notes on sediment transport and boil formation in ice-covered channels». *Proceedings of the 28<sup>th</sup> IAHR*, Graz, Austria, 22-27 August, 6 p.
- Falco, R. E. 1977. «Coherent motions in the outer region of turbulent boundary layers». *Physics of fluids*, vol. 20, s124-s132.
- Felix, M. 2002. «Flow structure of turbidity currents». *Sedimentology*, vol. 49, p. 397-419.
- Ferguson, R. I., A. D. Kirkbride et A. G. Roy. 1996. «Markov analysis of velocity fluctuations in gravel-bed rivers». In *Coherent Flow Structures in Open Channels*, sous la dir. de P. J. Ashworth, S. J. Bennett, J. L. Best et S. J. McLelland, p. 165-183. Chichester: John Wiley.
- Frothingham, K. M. et B. L. Rhoads. 2003. «Three-dimensional flow structure and channel change in an asymmetrical compound meander loop, Embarras river, Illinois». *Earth surface processes and landforms*, vol. 28, p. 625-644.

- Ghamry, H. K. et P. M. Steffler. 2002. «Effects of applying different distribution shapes for velocities and pressure on simulation of curved open channels». *Journal of hydraulic engineering*, vol. 128, p. 969-982.
- Goring, D. G. et V. I. Nikora. 2002. «Despiking acoustic Doppler velocimeter records». *Journal of hydraulic engineering*, vol. 128, p. 117-126.
- Grass, A. J. 1971. «Structural features of turbulent flow over smooth and rough boundaries». *Journal of fluid mechanics*, vol. 50, p. 233-255.
- Grass, A. J. et M. Mansour-Tehrani. 1996. «Generalized scaling of coherent bursting structures in the near-wall region of turbulent flow over smooth and rough boundaries». In *Coherent Flow Structures in Open Channels*, sous la dir. de P. J. Ashworth, S. J. Bennett, J. L. Best et S. J. McLelland, p. 41-61. Chichester: John Wiley.
- Grass, A. J., R. J. Stuart et M. Mansour-Tehrani. 1991. «Vortical structures and coherent motion in turbulent flow over smooth and rough boundaries», *Philosophical transaction of royal society of London A*, vol. 336, p. 29-47.
- Head, M. R. et P. Bandyopadhyay. 1981. «New aspects of turbulent boundary layer structure». *Journal of fluid mechanics*, vol. 107, p. 297-338.
- Hanjalic, K. et B. E. Launder. 1972. «Fully developed asymmetric flow in a plane channel». *Journal of fluid mechanics*, vol. 51, p. 301-335.
- Hardy, R. J., J. L. Best, S. N. Lane et P. E. Carbonneau. 2009. «Coherent flow structures in a depth-limited flow over a gravel surface: the role of near-bed turbulence and influence of Reynolds number». *Journal of geophysical research*, vol. 114 (F01003).
- Hurther, D. et U. Lemmin. 2001. «A correction method for turbulence measurements with a 3D acoustic Doppler velocity profiler». *Journal of atmospheric and oceanic technology*, vol. 18, p. 446-458.
- Kim, H. T., S. J. Kline et W. C. Reynolds. 1971. «The production of turbulence near a smooth wall in a turbulent boundary layer». *Journal of fluid mechanics*, vol. 50, p. 133-160.
- Kline, S. J., W. C. Reynolds, F. A. Schraub et P. W. Rundstadler. 1967. «The structure of turbulent boundary layer». *Journal of fluid mechanics*, vol. 30, p. 741-773.
- Lacy, J. R. et C. R. Sherwood. 2004. «Accuracy of a pulse-coherent acoustic Doppler profiler in a wave-dominated flow». *Journal of atmospheric and oceanic technology*, vol. 21, no 9, p. 1448-1461.

- Lane, S. N., P. M. Biron, K. F. Bradbrook, J. B. Butler, J. H. Chandler, M. D. Crowell, S. J. McLelland, K. S. Richards et A. G. Roy. 1998. «Three-dimensional measurement of river channel flow processes using acoustic Doppler velocimetry». *Earth surface processes and landforms*, vol. 23, p. 1247-1267.
- Lapointe, M. 1992. «Burst-like sediment suspension events in a sand bed river». *Earth surface processes and landforms*, vol. 17, p. 253-270.
- Larsen, P. A. 1969. «Head losses caused by an ice cover on open channels». *Journal of the Boston society of civil engineers*, vol. 56, no 1, p. 45-67.
- Leeder, M. R. 1983. «On the interactions between turbulent flow, sediment transport and bedform mechanics in channelized flow». In *Modern and ancient fluvial systems*, sous la dir. de J. D. Collinson et J. Lewin, 121-132. Coll. «Special Publication of the International Association of Sedimentologists», no 6. Oxford: Blackwell.
- Levasseur, M. 1999. «Turbulence de l'écoulement en présence de dunes fluviales». Mémoire de maîtrise, Montréal, Université de Montréal, 147 p.
- Lhermitte, R. et R. Serafin. 1984. «Pulse-to-pulse coherent Doppler sonar signal processing techniques». *Journal of atmospheric and oceanic technology*, vol. 1, no 4, p. 293-308.
- Lohrmann, A., B. Hackett, L. P. Roed. 1990. «High resolution measurements of turbulence, velocity and stress using a pulse-to-pulse coherent sonar». *Journal of atmospheric and oceanic technology*, vol. 7, p. 19-37.
- Markham, A. J. et C. R. Thorne. 1992a. «Geomorphology of gravel-bed river bends». In *Dynamics of Gravel-bed Rivers*, sous la dir. de P. Billi, R. D. Hey, C. R. Thorne et P. Tacconi, p. 433-450. Chichester: Wiley.
- Markham, A. J. et C. R. Thorne. 1992b. «Reply to discussion of geomorphology of gravel-bed river bends». In *Dynamics of Gravel-bed Rivers*, sous la dir. de P. Billi, R. D. Hey, C. R. Thorne et P. Tacconi, p. 452-456. Chichester: Wiley.
- Muste, M., K. Yu, T. Pratt et D. Abraham. 2004. «Practical aspects of ADCP data use for quantification of mean river flow characteristics; Part II: fixed-vessel measurements». *Flow measurement and instrumentation*, vol. 15, p. 17-28.
- Nakagawa, H. et I. Nezu. 1981. «Structure of space-time correlations of bursting phenomena in an open-channel flow». *Journal of fluid mechanics*, vol. 104, p. 1-43.
- Nezu, I. 2005. «Open channel flow turbulence and its research prospect in the 21<sup>st</sup> century». *Journal of hydraulic engineering*, vol. 131, no 4, p. 229-246.
- Nezu, I. et H. Nakagawa. 1993. *Turbulence in open-channel flows*, Rotterdam: Balkema, 281p.

- Nystrom, E. A. 2001. «Applicability of acoustic Doppler profilers to measurement of mean velocity and turbulence parameters». Mémoire de maîtrise, Urbana-Champaign, University of Illinois.
- Nystrom, E. A., C. R. Rehmann et K. A. Oberg. 2007. «Evaluation of mean velocity and turbulence measurements with ADCPs». *Journal of hydraulic engineering*, vol. 133, no 12, p. 1310-1318.
- Paiement-Paradis, G., G. Marquis et A. G. Roy. 2011. «Effects of turbulence on the transport of individual particles as bedload in a gravel-bed river». *Earth surface processes and landforms*, vol. 36, no 1, p. 107-116.
- Parthasarathy, R. N. et M. Muste. 1994. «Velocity measurements in asymmetric turbulent channel flows». *Journal of hydraulic engineering*, vol. 120, no 9, p. 1000-1020.
- Perry, A. E. et M. S. Chong. 1982. «On the mechanism of wall turbulence». *Journal of fluid mechanics*, vol. 119, p. 173-217.
- Robinson, S. K. 1991. «Coherent motions in the turbulent boundary layer». *Annual review of fluid mechanics*, vol. 23, p. 601-639.
- Roy, Y. M. et R. F. Blackwelder. 1994. «On the role of the outer regions in the turbulent-boundary –layer bursting process». *Journal of fluid mechanics*, vol. 259, p. 345-373.
- Roy, A. G., T. Buffin-Bélanger et S. Deland. 1996. «Scales of turbulent coherent flow structures in a gravel bed river». In *Coherent Flow Structures in Open Channels*, sous la dir. de P. J. Ashworth, S. J. Bennett, J. L. Best et S. J. McLelland, p. 147-164. Chichester: John Wiley.
- Roy, A. G., T. Buffin-Bélanger, H. Lamarre et A. D. Kirkbride. 2004. «Size, shape and dynamics of large-scale turbulent flow structures in a gravel-bed river». *Journal of fluid mechanics*, vol. 500, p. 1-27.
- Rozovskii, I. L. 1954. «Concerning the question of velocity distribution in stream bends». DAN URSR Report of the Academy of Sciences of the Ukraine SSR, 1.
- Schvidchenko, A. B. et G. Pender. 2001. «Macroturbulent structure of open-channel flow over gravel beds». *Water resources research*, vol. 37, p. 709-719.
- Smith, C. R. 1996. «Coherent flow structures in smooth-wall turbulent boundary layers: facts, mechanisms and speculation». In *Coherent Flow Structures in Open Channels*, sous la dir. de P. J. Ashworth, S. J. Bennett, J. L. Best et S. J. McLelland, p. 1-32. Chichester: John Wiley.
- Smith, C. R., D. J. A. Walker, A. H. Haidari et U. Sobrun. 1991. «On the dynamics of near-wall turbulence». *Philosophical transactions royal society of London A*, vol. 336, p. 131-175.

SonTek. 2004. *PC-ADP - Read Me First!, SonTek PC-ADP manual*, San Diego, California, 28p.

Sukhodolov, A., M. Thiele, H. Bungartz et C. Engelhardt. 1999. «Turbulence structure in an ice-covered, sand-bed river». *Water resources research*, vol. 35, no 3, p. 889-894.

Sui, J., J. Wang, R. Balachandar, Z. Sun et D. Wang. 2008. «Accumulation of frazil ice along a river bend». *Canadian journal of civil engineering*, vol. 35, p. 158-169.

Taylor, G. I. 1935. «Statistical theory of turbulence». *Proceedings of the royal society of London A*, vol. 151, p. 421-454.

Thomson, J. 1876. «On the origin of windings of rivers in alluvial plains, with remarks on the flow of water round bends in pipes». *Proceedings of the royal society of London*, vol. 25, p. 5-8.

Tilston, M. et P. M. Biron. 2006. «Structure de l'écoulement tridimensionnel, turbulence et contrainte de cisaillement dans une boucle de méandre». *Géographie physique et quaternaire*, vol. 60, no 3, p. 225-239.

Urroz, G. E. 1988. «Studies on ice jams in river bends». Thèse de doctorat, Iowa City, The University of Iowa, 243 p.

Urroz, G. E. et R. Ettema. 1994. «Application of two-layer hypothesis to fully developed flow in ice-covered curved channels». *Canadian journal of civil engineering*, vol. 21, p. 101-110.

Voulgaris, G. et J. H. Trowbridge. 1998. «Evaluation of the acoustic Doppler velocimeter (ADV) for turbulence measurements». *Journal of atmospheric and oceanic technology*, vol. 15, no 1, p. 272-289.

Zufelt, J. 1988. «A laboratory study of transverse velocities and ice jamming in a river bend», *Proceedings of the International Association of Hydraulic Research Ice Symposium*, Hokkaido, Japan, p. 189-197.

